Two populations of cytoplasmic dynein contribute to spindle positioning in *C. elegans* embryos

Ruben Schmidt,[1,2] Lars-Eric Fielmich,[1] Ilya Grigoriev,[2] Eugene A. Katrukha,[2] Anna Akhmanova,[2] and Sander van den Heuvel[1]

[1]Developmental Biology, Department of Biology, Faculty of Sciences and [2]Cell Biology, Department of Biology, Faculty of Sciences, Utrecht University, Utrecht, Netherlands

The position of the mitotic spindle is tightly controlled in animal cells as it determines the plane and orientation of cell division. Contacts between cytoplasmic dynein and astral microtubules (MTs) at the cell cortex generate pulling forces that position the spindle. An evolutionarily conserved Gα-GPR-1/2$^{Pins/LGN}$–LIN-5$^{Mud/NuMA}$ cortical complex interacts with dynein and is required for pulling force generation, but the dynamics of this process remain unclear. In this study, by fluorescently labeling endogenous proteins in *Caenorhabditis elegans* embryos, we show that dynein exists in two distinct cortical populations. One population directly depends on LIN-5, whereas the other is concentrated at MT plus ends and depends on end-binding (EB) proteins. Knockout mutants lacking all EBs are viable and fertile and display normal pulling forces and spindle positioning. However, EB protein–dependent dynein plus end tracking was found to contribute to force generation in embryos with a partially perturbed dynein function, indicating the existence of two mechanisms that together create a highly robust force-generating system.

Introduction

The mitotic spindle dictates the plane of cell cleavage through its position and interactions with the cell cortex (Galli and van den Heuvel, 2008; Morin and Bellaïche, 2011). Therefore, the position of the spindle determines the relative size and location of daughter cells and controls whether polarized cells divide symmetrically or asymmetrically. Thus, accurate positioning of the spindle is critical for a wide range of processes that include maintenance of tissue integrity, creation of different cell types, and coordination of stem cell proliferation and differentiation.

The *Caenorhabditis elegans* early embryo provides an important in vivo model for studies of spindle position regulation. The one-cell embryo divides asymmetrically based on an anterior–posterior (A-P) polarity axis established after fertilization (Rose and Gönczy, 2014). Spindle severing experiments revealed that pulling forces acting from the cell cortex on astral microtubules (MTs) position the spindle and are higher in the posterior than in the anterior (Grill et al., 2001). This pulling force asymmetry leads to posterior displacement of the spindle and allows cell cleavage to create two blastomeres of unequal size and developmental fate.

Genetic screens and biochemical experiments have revealed a variety of factors that control cortical pulling forces. Among these are the evolutionarily conserved proteins Gα, GPR-1/2$^{Pins/LGN}$, and LIN-5$^{Mud/NuMA}$ (Lorson et al., 2000; Gotta and Ahringer, 2001; Colombo et al., 2003; Gotta et al., 2003; Srinivasan et al., 2003). These proteins are needed to form the force generator complex (FGC), which also includes cytoplasmic dynein (Nguyen-Ngoc et al., 2007). This large multisubunit protein complex is the major minus end–directed motor in cells and is essential for a large variety of cellular processes (Kardon and Vale, 2009). In the current model, dynein is recruited to the cell cortex either directly or indirectly via an extended N-terminal region of LIN-5 (Kotak et al., 2012). Dynein then associates with astral MTs in an end-on configuration, inducing pulling forces via both MT depolymerization and minus end–directed movement. Both in vivo and in vitro studies support this model (Nguyen-Ngoc et al., 2007; Gusnowski and Srayko, 2011; Hendricks et al., 2012; Laan et al., 2012).

It remains unclear, however, how dynein is recruited to the cortex and how MT dynamics are coupled to force generation and mitotic spindle positioning. MT growth and shrinkage are spatiotemporally modulated by a large variety of MT-associated proteins, a subset of which concentrates at the growing MT plus end (Akhmanova and Steinmetz, 2015). These MT plus end–tracking proteins (+TIPs) form a highly interconnected and dynamic network, which is regulated in a cell cycle– and position–dependent manner to fine-tune MT dynamics (Honnappa et al., 2006; Zimniak et al., 2009; Ferreira et al., 2013; Tamura et al., 2015). Members of the end-binding (EB) protein family are seen as master regulators of the +TIP network, as they bind

Correspondence to Sander van den Heuvel: s.j.l.vandenHeuvel@uu.nl; Anna Akhmanova: a.akhmanova@uu.nl

Abbreviations used: +TIP, plus end–tracking protein; A-P, anterior–posterior; DIC, differential interference contrast; EB, end-binding; FGC, force generator complex; FP, fluorescent protein; MT, microtubule; SDCM, spinning-disk confocal fluorescence microscopy; TIRF, total internal reflection fluorescence; ts, temperature-sensitive.

The Rockefeller University Press
J. Cell Biol. Vol. 216 No. 9 2777–2793
https://doi.org/10.1083/jcb.201607038

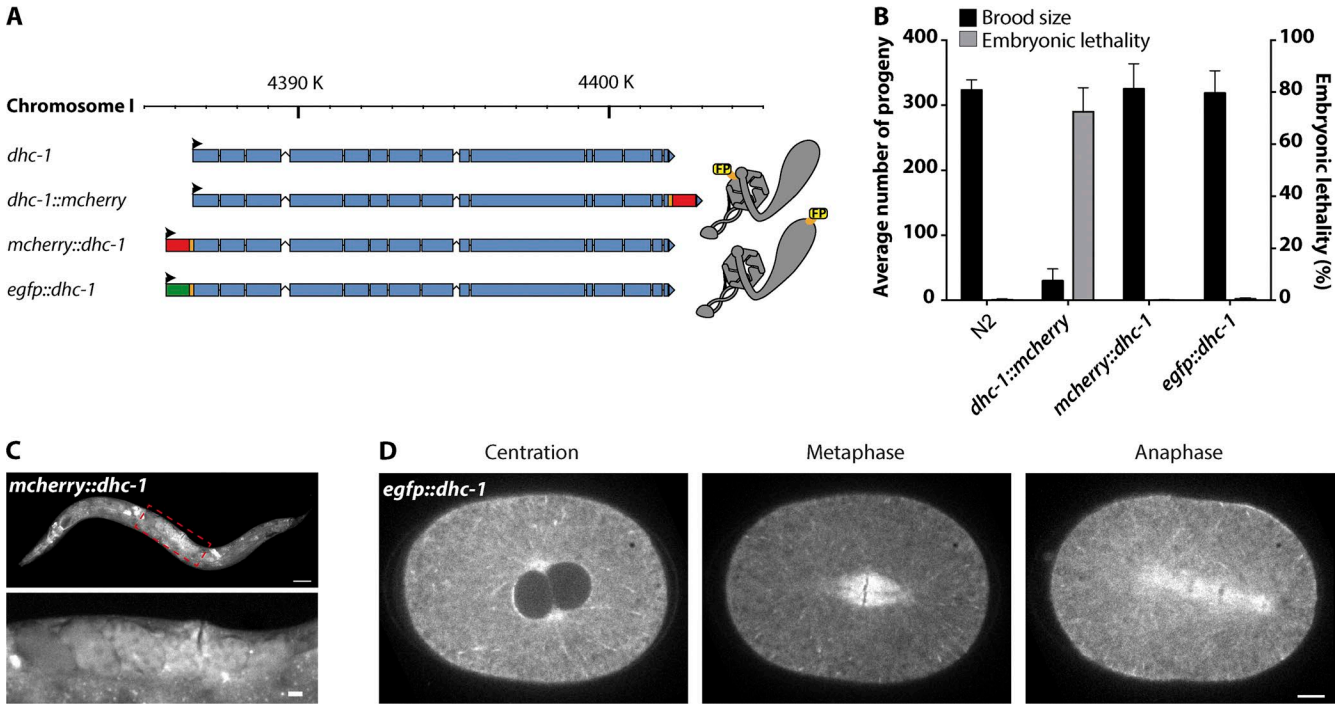

Figure 1. **Endogenous tagging of *dhc-1*.** (A) Dynein tagging strategies. Colors indicate *dhc-1* exons (blue), *mcherry* (red), *egfp* (green), and linkers (orange). Cartoons illustrate dynein heavy chain with FP fused to the C (top) or N terminus (bottom). (B) Brood size and embryonic lethality of *dhc-1* knock-in strains shown as means ± SD. $n = 4$ animals each. (C) Widefield image showing mCherry::DHC-1 expression in an adult with a zoom of the germline (red dashed box) below. Bars: (top) 50 µm; (bottom) 10 µm. (D) SDCM images of eGFP::DHC-1 localization in the one-cell embryo. Bar, 5 µm.

autonomously to the growing MT end and recruit multiple other +TIPs (Honnappa et al., 2006; Bieling et al., 2007; Maurer et al., 2012; Akhmanova and Steinmetz, 2015; Zhang et al., 2015b).

Dynein is known to behave as a +TIP in a variety of cellular contexts (Vaughan et al., 1999; Han et al., 2001; Lenz et al., 2006; Kobayashi and Murayama, 2009). In mammals, this is classically regarded as part of a "search and capture" mechanism, by which the complex finds cargo molecules via the MT plus end before initiating transport (Kirschner and Mitchison, 1986; Vaughan et al., 2002). Interactions between EB1, CLIP-170, and the dynactin protein p150Glued recruit the human dynein complex to the MT plus end (Berrueta et al., 1999; Lansbergen et al., 2004; Duellberg et al., 2014). In the budding yeast *Saccharomyces cerevisiae*, dynein plus end tracking is coupled to offloading at the cortex and association of dynein with its cortical anchor Num1 (Lee et al., 2003; Sheeman et al., 2003; Markus and Lee, 2011). Disruption of dynein plus end recruitment is thus associated with spindle positioning defects in yeast, but whether this applies to animals remains to be determined.

In this study, we explore the localization of dynein during mitotic pulling force generation in the one-cell *C. elegans* embryo. Fluorescent protein (FP) tagging of endogenous dynein helped reveal two cortical populations, one enriched at MT plus ends depending on EB protein 2 (EBP-2) along with an MT-independent population recruited by LIN-5. The LIN-5–dependent dynein population exhibited significant asymmetry in cortical retention, governed by PAR polarity. This indicates that a subpopulation of LIN-5 is dynein associated and differentially regulated. We created single-, double-, and triple-deletion mutants of EB family genes and found that spindle positioning and embryonic development can proceed as normal in the absence of dynein plus end tracking. However, plus end tracking appeared to provide a backup mechanism to ensure robust force generation when dynein function was partially perturbed.

Results

Visualization of the endogenous dynein complex

We applied a CRISPR/Cas9-assisted knock-in strategy to visualize the dynamics of cytoplasmic dynein in the early *C. elegans* embryo. To label all possible compositions of the dynein complex, we added an FP to the dynein heavy chain, encoded by *dhc-1* in *C. elegans* (Fig. 1 A). To allow for functional comparison, we inserted *mcherry* directly upstream of the *dhc-1* stop codon, and we also inserted *mcherry* or *egfp* directly upstream of the *dhc-1* start codon. A glycine linker was inserted between FPs and *dhc-1* to preserve independent protein folding (Fig. 1 A).

Multiple homozygous viable knock-in strains were obtained with N- or C-terminal DHC-1 protein fusions. However, C-terminal tagging of *dhc-1* caused severe embryonic lethality and a reduced brood size (Fig. 1 B). Differential interference contrast (DIC) microscopy revealed spindle positioning and cell division defects from the one-cell stage onward in two independent strains. These defects are in accordance with perturbed dynein function (Schmidt et al., 2005). We concluded that C-terminal tagging of endogenous DHC-1 causes partial loss of function and did not further study dynein in these strains. Homozygous larvae with N-terminally tagged DHC-1 were fully viable, produced a normal brood size (Fig. 1 B), and appeared healthy during all stages of development. Thus, N-terminal tagging of DHC-1 with mCherry or eGFP does not perturb dynein function.

Epifluorescence microscopy revealed that mCherry::DHC-1 and eGFP::DHC-1 are expressed in all somatic tissues and in the germline (Fig. 1 C, zoomed image). After imaging early embryos by spinning-disk confocal fluorescence microscopy (SDCM), DHC-1 was detected in the cytoplasm during all stages of the cell cycle and localized specifically to the nuclear envelope, centrosomes, kinetochores, kinetochore MTs, central spindle, astral MTs, and the cell cortex during mitosis (Fig. 1 D). This localization pattern is in accordance with previous immunohistochemistry and overexpression studies (Schmidt et al., 2005; Nguyen-Ngoc et al., 2007; Gassmann et al., 2008; Kimura and Kimura, 2011). In addition, we noticed cometlike accumulations of dynein radiating from the centrosomes to the cell periphery in a pattern that appeared to follow the mitotic astral MT network.

Dynein tracks MT plus ends during mitosis

To further explore the dynein localization pattern, P*pie-1*::*gfp::tbb-2*$^{\beta\text{-tubulin}}$ (Praitis et al., 2001) was coexpressed with *mcherry::dhc-1* and imaged in embryos. Dynein comets were clearly MT associated (Fig. 2 A, arrow, and Video 1). Because dynein is a minus end–directed motor protein, cortex-directed dynein comets may represent a plus end tracking population. To examine this possibility, we coexpressed *mcherry::dhc-1* with P*pie-1::ebp-2::gfp* (Srayko et al., 2005; Kozlowski et al., 2007). This revealed a strong overlap between dynein and EBP-2::GFP comets (Fig. 2, B and C; and Video 2). Moreover, the velocities of mCherry::DHC-1 and EBP-2::GFP comets were almost identical (Fig. 2 D) and agree with previous measurements of MT growth speeds during metaphase (0.72 ± 0.02 µm/s; Srayko et al., 2005). Dynein accumulation at MT plus ends appears to be a general feature of mitotic animal cells, as we also observed this in HeLa cells stably expressing labeled dynein intermediate chain 2 (DIC2-GFP; Poser et al., 2008; Splinter et al., 2012). Moreover, we observed MT plus end tracking of dynein in later stages of *C. elegans* embryos (Fig. S1, A and B) as well as overlap between dynactin components GFP::DNC-1$^{\text{p150Glued}}$ and GFP::DNC-2$^{\text{p50/dynamitin}}$ and mCherry::DHC-1 comets (Fig. S2 A). Collectively, our data show that the endogenous dynein complex tracks MT plus ends.

Next, we addressed whether MT plus end tracking of the dynein complex relates to pulling force generation. Using dual-color total internal reflection fluorescence (TIRF) microscopy, we observed simultaneous appearance and strong colocalization of dynein comets with end-on MT plus end–cortex contacts in mitosis (Fig. 2, E–G; and Videos 3 and 4). Interestingly, the concentrated mCherry::DHC-1 signal dissipated when MTs stopped growing, as judged by the loss of EBP-2::GFP signal, suggesting that the majority of dynein molecules are released.

To image dynein comets during cortical force generation, we focused on invaginations of the plasma membrane, which appear to visualize individual force generation events (Redemann et al., 2010). To readily detect such invaginations, we created a reporter strain with single copy–integrated PH::eGFP expressed from the general *eft-3* promoter. Dual-color imaging of PH::eGFP and mCherry::DHC-1 revealed frequent co-occurrence of dynein comets reaching the cortex and emergence of membrane invaginations (13/25 events; Fig. 2 H and Video 5). However, there was no enrichment of dynein after the initiation of invaginations. This confirms that a significant part of the dynein population present at the MT plus end dissipates upon membrane contact and likely does not contribute to pulling forces.

EBs and dynein plus end tracking are not required for development and spindle positioning

To examine its contribution in cortical pulling forces, we decided to disrupt dynein plus end accumulation by removing EBs. Two homologues of mammalian EBs, EBP-1 and EBP-2, exhibit plus end tracking activity when overexpressed in the *C. elegans* embryo (Srayko et al., 2005). An annotated third homologue, *ebp-3*, has likely arisen by duplication of the genomic region containing the *ebp-1* gene, and their nearly identical DNA sequences suggest that this was a recent event. However, the predicted EBP-3 protein lacks the calponin homology domain, which is required for recognition of the MT plus end (Slep and Vale, 2007; Maurer et al., 2012). Although we suspect that *ebp-3* is a pseudogene, we will refer to the *ebp-1* and *ebp-3* genes collectively as *ebp-1/3*.

Knockdown of *ebp-1/3* by RNAi did not appear to affect eGFP::DHC-1 plus end tracking. In contrast, loss of *ebp-2* expression abolished the appearance of dynein comets (Fig. 3 A). Interestingly, this did not result in obvious spindle positioning or cell division defects. As RNAi knockdown probably is incomplete, we used CRISPR/Cas9 to create knockout alleles for both *ebp-2* and *ebp-1/3* (Fig. 3 B). The *ebp-1* and *ebp-3* genes were removed together by excision of a ∼17-kb region. For *ebp-2,* the coding region and ∼1 kb upstream of the start codon was deleted. Both the *Δebp-1/3* and *Δebp-2* strains could be stably maintained as homozygotes, indicating that neither *ebp-1/3* nor *ebp-2* is required for normal development and reproduction.

The *ebp* deletion mutants closely resembled the RNAi embryos in dynein localization. In Δ*ebp-1/3* embryos, dynein still localized to the MT plus ends, whereas this localization was completely absent in *Δebp-2* embryos (Fig. 3 C and Video 6). In contrast, dynein localization to the nuclear envelope, spindle midzone, and poles did not appear to be affected in either case, which indicates that dynein depends on EBP-2 specifically for recruitment to MT plus ends (Fig. S2, C–E).

Although general development was normal, *Δebp-1/3* caused a slight reduction in brood size and a slight increase in embryonic lethality (Fig. 3 D). Surprisingly, *Δebp-1/2/3* animals were viable and could be maintained as triple-homozygous mutants, showing that development and reproduction can proceed in the absence of EBs. Triple mutants showed a stronger reduction in brood size than *Δebp-1/3* animals, which indicated some redundancy among the EBs. Embryonic lethality remained low, which is remarkable given the expected profound disruption of the +TIP network. Although *Δebp-1/2/3* larvae generally did not show developmental defects, we observed a low penetrant pleiotropic phenotype among adults. This included a low frequency of dumpy, sterile, and/or uncoordinated animals as well as nonviable larvae that exploded through the vulva. In addition, some triple mutant adults developed irregularities that seemed epidermal bulges. Because of the very low penetrance, we did not further examine these abnormalities.

Next, we assessed whether spindle positioning was affected in *ebp*-deletion mutants. Importantly, asymmetric positioning of the spindle and subsequent asymmetric division of the one-cell embryo was not affected in any of the mutants (Fig. S3 A). *Δebp-1/2/3* embryos exhibited a slightly rounder shape compared with WT embryos (Fig. S3 B). The position

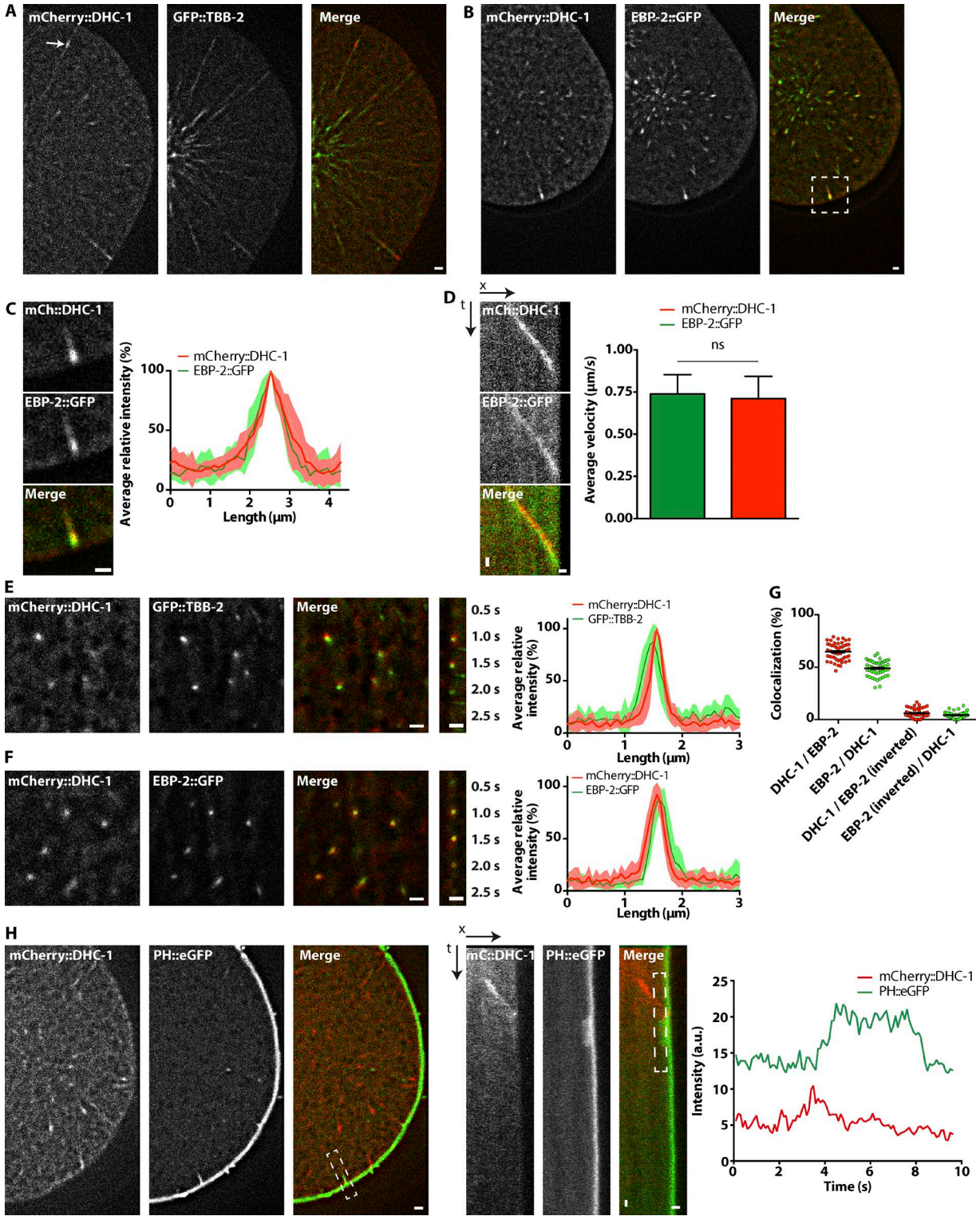

Figure 2. **Dynein tracks MT plus ends during mitosis.** (A and B) SDCM images of embryos expressing mCherry::DHC-1 and GFP::TBB-2 (A) or EBP-2::GFP (B). The arrow indicates dynein at the plus end. The white box indicates the zoomed image in C. (C) Intensity profiles of mCherry::DHC-1 and EBP-2::GFP comets shown as percentages of maximum. Means ± SD are shown. n = 10. (D) Kymographs (left) and mean velocities (right) of metaphase comets; mCherry::DHC-1 (n = 57) and EBP-2::GFP (n = 116) means ± SD. Unpaired Welch's Student's t test; not significant. (E and F) TIRF images of early anaphase mCherry::DHC-1 and GFP::TBB-2 (E) or EBP-2::GFP (F) localization. Graphs show intensity profiles as mean (n = 10) percentage of maximum ± SD. (G) Quantification of EBP-2::GFP and mCherry::DHC-1 colocalization as in F, shown as means ± SEM of per frame percentage colocalization of 2,351 mCherry::DHC-1 and 3,178 EBP-2::GFP particles from three embryos. (H) SDCM images of anaphase mCherry::DHC-1 and PH::eGFP localization. The leftmost three panels are kymographs of the invagination indicated in the third panel from the right (white dashed box). Graph shows intensity profiles as measured along the box in the rightmost panel, representative of n = 25 events. Bars: (horizontal) 1 µm; (vertical) 1 s.

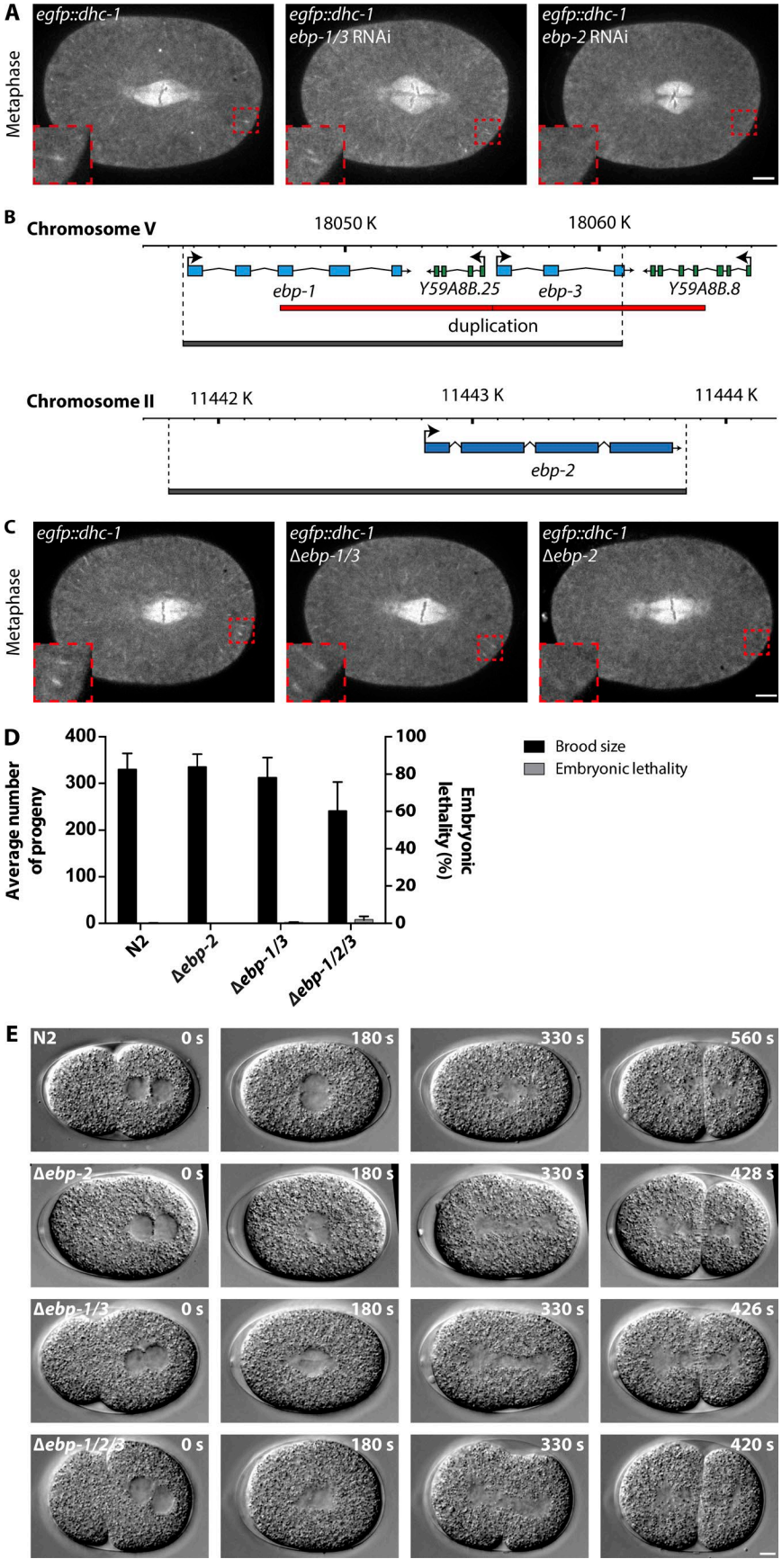

Figure 3. **Analysis of dynein plus end tracking and development of Δ*ebp* mutants.** (A) SDCM images illustrating eGFP::DHC-1 localization in WT, *ebp-1/3(RNAi)*, and *ebp-2(RNAi)* embryos. Insets highlight the presence or absence of dynein comets. (B) *ebp-1/3* and *ebp-2* knockout strategies. Relevant genes are shown in blue and green, genetic duplication is in red, and genetic deletions are in gray. (C) SDCM images illustrating eGFP::DHC-1 localization in WT, *Δebp-2*, and *Δebp-1/3* embryos. Insets highlight the presence or absence of dynein comets. (D) Embryonic lethality and brood size of *Δebp* mutants shown as means ± SD. $n = 4$ animals each. (E) DIC images of N2, *Δebp-2*, *Δebp-1/3*, and *Δebp-1/2/3* one-cell embryos. Time past pronuclear meeting ($t = 0$) is indicated in seconds. Bar, 5 µm.

of pronuclear meeting did not change significantly (Fig. S3 C), whereas centration of the nucleocentrosomal complex occurred slightly more posterior in each mutant (Fig. S3 D). Spindles formed along the long axis as normal (Fig. S3 E), whereas their elongation during anaphase was slightly increased in *Δebp-1/2/3* embryos (Fig. S3 F). Regardless of these small deviations, the outcome of mitosis was not affected. However, all *Δebp* strains showed accelerated progression through mitosis (Fig. 3 E, Fig. S3 G, and Video 7). This was observed in *Δebp-1/3* and *Δebp-2* embryos but was most dramatic in *Δebp-1/2/3* mutants. Both the progression from pronuclear meeting to nuclear envelope breakdown and the time between the start of chromosome segregation and cytokinesis were significantly faster than normal (Fig. S3, G–J). However, there was no significant reduction in the time between nuclear envelop breakdown and anaphase onset (Fig. S3 I), indicating that the accelerated mitosis does not result from bypassing or premature satisfaction of the spindle assembly checkpoint.

EBs and dynein plus end tracking are not required for cortical pulling forces

We quantified the amplitudes of spindle pole movements during anaphase as a first readout for cortical force generation (Pecreaux et al., 2006). Interestingly, spindle rocking was generally not affected by the removal of EBs. The posterior pole showed a slight but significant increase in maximum amplitude in the *Δebp-1/3* background, but this was not observed in *Δebp-1/2/3* mutants (Fig. 4 A).

To more directly quantify cortical pulling forces during spindle displacement, we performed spindle severing assays with a focused UV laser beam (Grill et al., 2001). Upon severing the spindle during anaphase onset, the centrosomes separated with a velocity proportional to the net forces acting on their astral MTs (Fig. 4 B and Video 9; Grill et al., 2001). Remarkably, all *Δebp* mutants assembled apparently normal mitotic spindles and showed normal spindle pole peak velocities (Fig. 4 C). Thus, cortical pulling force generation during spindle positioning is largely unaltered in the absence of EB proteins.

In addition to recruiting proteins to the MT plus end, EB proteins affect MT dynamics (Komarova et al., 2009; Zanic et al., 2013; Maurer et al., 2014; Zhang et al., 2015b). However, the effect of complete loss of EB family members on MT dynamics has not been reported in vivo. A hurdle for studying MT dynamics in the one-cell worm embryo is the extremely dense MT network (Kozlowski et al., 2007). Therefore, we imaged labeled MTs at the cortex by TIRF microscopy and quantified the duration of end-on MT–cortex contacts during spindle displacement (Fig. 4 D). This revealed a slight increase in mean residence time in all *Δebp* mutants, of which only *Δebp-2* was significantly different from WT, whereas the mean density of cortical MT contacts remained constant (Fig. 4 E and Video 10). This indicates that loss of EBP-2 either reduces MT growth rate, catastrophe frequency, or both, thereby allowing prolonged contact with the cell cortex. Interestingly, *Δebp-2* and *Δebp-1/2/3* embryos also exhibited reduced midzone MT densities (Fig. S4, A–C), which led to full or partial bisection of spindles during anaphase and could be caused by altered MT dynamics. This phenotype is reminiscent of *spd-1*^{PRC1} loss of function, which diminishes the mechanical strength of the midzone by loss of MT bundling (Verbrugghe and White, 2004). In addition, the intensity profile of the metaphase astral MT network was slightly steeper in *Δebp-2* and *Δebp-1/2/3* mutants compared with controls (Fig. 4 F), indicating that the distribution of MT length was mildly altered. Collectively, these results indicate that complete loss of EBs has a mild effect on MT organization and dynamics in vivo, but does not significantly change spindle assembly and positioning.

LIN-5 recruits dynein to the cell cortex independent of MT plus end tracking

If dynein plus end tracking is not required for spindle positioning, then how does dynein reach the cortex? Previous studies have visualized cortical dynein localization by immunohistochemistry (Nguyen-Ngoc et al., 2007; Kotak et al., 2012). Although cortical dynein could be observed in two-cell embryos, staining of one-cell embryos did not show clear cortical localization. Time-lapse SDCM of eGFP::DHC-1 zygotes revealed no measurable enrichment of dynein at the cortex over cytoplasmic values during metaphase spindle displacement, similar to *lin-5(RNAi)* embryos (Fig. 5 A). However, we observed transient regions of DHC-1 enrichment in cortical patches during late anaphase (Fig. 5 B). These patches were most pronounced at the posterior cortex during spindle rocking and often followed the oscillatory behavior of the spindle poles (Fig. S4, D and E). This indicates that spindle pole proximity and cortical dynein recruitment could be coupled like they are in mammalian cells (Kiyomitsu and Cheeseman, 2012). The cortical enrichment of dynein was not perturbed in *Δebp-1/3* or *Δebp-2* mutant embryos. In contrast, *lin-5(RNAi)* abolished cortical dynein localization but did not affect its plus end tracking (Fig. 5 B). Thus, EBP-2 and EBP-1/3 are not required for the cortical localization of dynein during anaphase, which fully depends on LIN-5.

To explore the relative cortical localization patterns of LIN-5 and dynein, *egfp::lin-5; mcherry::dhc-1* embryos were imaged by SDCM (Fig. 5 C). In late metaphase, eGFP::LIN-5 became modestly enriched at the cortex as compared with the adjacent cytoplasm, both in the anterior and posterior. Although this was not observed for dynein (Fig. 5, A and C), both LIN-5 and dynein showed higher cytoplasmic levels in the anterior compared with the posterior during all mitotic stages (Fig. S5 A). This gradient affected the relative cortex/cytoplasm ratios calculated for the anterior and posterior and caused the increase of cortical levels observed in the posterior, which was not observed when a mean cytoplasmic value was used for normalization of all points instead (Fig. S5 A).

During anaphase, cortical enrichment of eGFP::LIN-5 increased substantially, most noticeably in the posterior. When averaging fluorescence intensities from multiple embryos, mCherry::DHC-1 did not show clear enrichment at the cortex above local cytoplasmic levels during anaphase. This reflects the patchy appearance of cortical dynein enrichment along the A-P axis (Fig. 5 C; also see Fig. 5 B). Importantly, side-by-side comparison of nonnormalized cortical line scans revealed a strong cross-correlation between cortical eGFP::LIN-5 and mCherry::DHC-1 (Fig. 5 C; examples in Fig. S5 B). This indicates that both proteins follow a similar cortical distribution, in agreement with LIN-5–dependent dynein localization. These protein localization patterns can account for force asymmetries in anaphase, but not during metaphase spindle displacement.

In a previous study, we observed cortical dynein localization in the absence of astral MTs (Portegijs et al., 2016). We repeated this experiment for *egfp::dhc-1* and *mcherry::dhc-1; egfp::lin-5* embryos permeabilized by *perm-1* RNAi treatment and exposed to 1 µM nocodazole (Carvalho et al., 2011; Berends

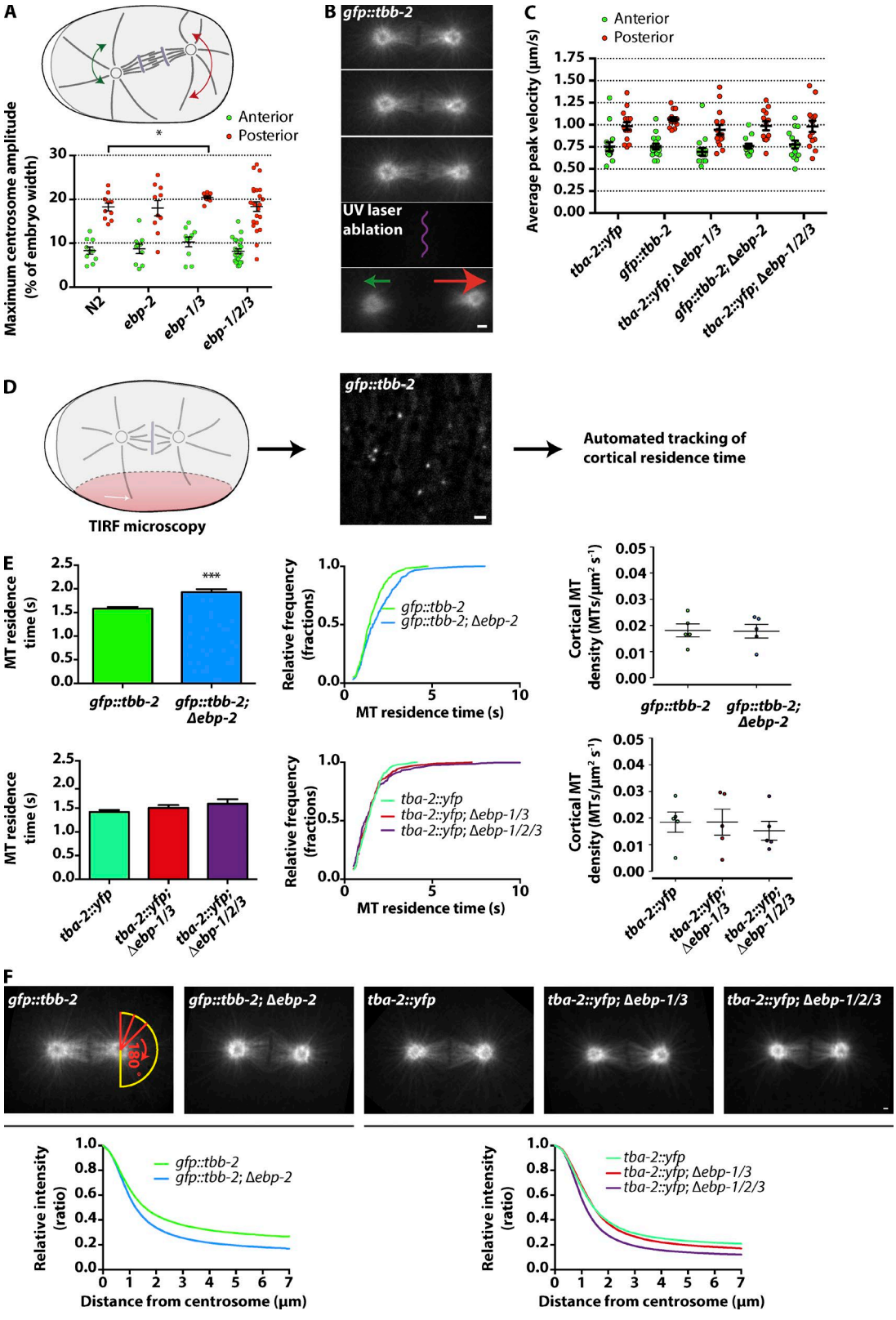

Figure 4. **Loss of EBP-1/2/3 mildly affects MT dynamics and does not perturb normal mitotic pulling force generation.** (A) Quantification of anaphase centrosome rocking in WT and *Δebp* embryos. Maximum amplitudes are shown as means ± SEM. Unpaired Welch's Student's *t* test; *, $P < 0.05$. $n = 10–23$. (B) Example of spindle severing with a UV laser (purple) in a GFP::TBB-2 embryo. Arrows indicate the direction and relative speed of centrosome displacement upon bisection. (C) Quantification of centrosome velocities upon spindle severing in WT and *Δebp* embryos shown as means ± SEM. Unpaired Welch's Student's *t* test. $n = 13–15$. (D) Method for quantification of cortical MT residence time by TIRF microscopy of embryos expressing fluorescent tubulin. (E) Quantifications as illustrated in D for control and *Δebp* embryos. Bars represent means ± SEM. Mann–Whitney *U* test; ***, $P < 0.001$. $233 \leq n \leq 343$ events from five embryos for each condition. Graphs show cumulative relative fractions of residence time distributions. Right graphs show density

et al., 2013). The use of tubulin and EBP-2 markers confirmed the absence of astral MTs, whereas the presence of a spindle remnant revealed cells in mitosis (Fig. 5 D, arrow). Dynein still localized to the cortex during mitosis in these embryos, and this localization strongly overlapped with and depended on LIN-5 (Fig. 5 D). Thus, LIN-5 recruits dynein to the cell cortex during mitosis, which can occur directly from the cytoplasm and in the absence of astral MTs.

As SDCM did not reliably detect dynein at the cortex during metaphase, we visualized cortical eGFP::DHC-1 more selectively at this stage by TIRF microscopy. Notably, this revealed two cortical populations of dynein that could be genetically separated. One population was detected as bright fluorescent spots that were absent in the *Δebp-2* background and thus represented dynein comets at the cell cortex (Fig. 6 A, arrow). A second population consisted of relatively dim spots that were absent in *lin-5(RNAi)* embryos (Fig. 6 A, arrowhead). Most notably, *Δebp-2; lin-5(RNAi)* embryos showed almost complete loss of detectable cortical dynein (Fig. 6 A and Video 8). Furthermore, the increase in dynein levels associated with MT plus ends at the cortex in *lin-5(RNAi)* embryos may indicate that the cortex and MT plus ends compete for dynein binding or that LIN-5 suppresses dynein plus end accumulation (relative cumulative distribution in Fig. 6 B and sum of intensities in Fig. 6 C). Thus, two populations of dynein are present at the cortex in metaphase: an EBP-2–dependent plus end tracking population and a LIN-5–dependent cortical population. As shown in Fig. 5 D, LIN-5 can most likely recruit dynein directly from the cytoplasm to the cortex, which would explain why plus end tracking of dynein is not required for its cortical localization during mitosis.

To investigate whether the cortical populations of dynein and LIN-5 show asymmetries that relate to asymmetric spindle positioning, we examined their dynamics by time-lapse TIRF microscopy combined with FRAP analysis. To this end, eGFP::DHC-1 and eGFP::LIN-5 embryos were photobleached in regions in the anterior and posterior, after which recovery of fluorescence was recorded during a 30-s timespan relevant for spindle positioning (Fig. 6 D). Overall, LIN-5 recovered more quickly than dynein in WT as well as in Δ*ebp-2* embryos (Fig. 6, E–G; and Table S2). As dissociation of LIN-5 also removes dynein, more stable cortical retention of dynein compared with LIN-5 would not be expected. However, statistical analyses indicated that the averaged eGFP::LIN-5 and eGFP::DHC-1 fluorescence recovery curves are most reliably fit by two-phase nonlinear regression analysis (extra sum-of-squares F test one- vs. two-phase fit; ****, $P < 0.0001$). The half-lives of the fast phases of cortical eGFP::LIN-5 and eGFP::DHC-1 recovery were similar to the recovery half-life of the corresponding proteins in the cytoplasm (Figs. 6 F and S5 D). This probably reflects that our FRAP measurements include a cytoplasmic protein fraction or alternatively that part of the cortical population exchanges at a speed similar to cytoplasmic diffusion. The contribution of the fast phase was larger for LIN-5 recovery compared with DHC-1, which contributed to the faster overall recovery of LIN-5 (Fig. 6 G).

Importantly, the half-lives for the slow phase of recovery were similar for LIN-5 and dynein (Fig. 6 F, colored bars). Thus, this phase likely reflects the dynamics of a LIN-5–bound dynein population at the cortex. In addition to a fast and slow recovering phase, a small protein fraction remained immobile within the 30-s interval. Interestingly, individual fits revealed a statistically larger immobile fraction of eGFP::DHC-1 in the posterior compared with the anterior (Fig. 6, G and H). This difference also appeared detectable for eGFP::LIN-5 but was not significant (Fig. 6, G and H). FRAP analysis of eGPF::DHC-1 in *Δebp-2* embryos also showed asymmetry in dynein dynamics, indicating that the asymmetry resides in the LIN-5–dependent cortical dynein population, as detected in Fig. 6 (A–C). Notably, the FRAP curves of *Δebp-2* embryos showed higher recovery than WT (Fig. 6 E), even extending beyond 100% (Fig. 6 H). This may be attributed to the faster progression through mitosis in *Δebp-2* embryos (Fig. S3, G–J) in combination with an increase in cortical dynein during mitosis from metaphase onwards. Nevertheless, extrapolation of the curves confirmed a higher percentage recovery in the anterior compared with posterior of *Δebp-2* embryos, similar to WT eGFP::DHC-1 embryos (Fig. 6 H). Disruption of polarity by knockdown of *par-2* or *par-3* abolished the observed asymmetry in cortical eGFP::DHC-1 recovery (Fig. 6, E and H).

In summary, the obtained FRAP curves probably result from combined measurements of dynein in the cytoplasm and LIN-5–associated dynein at the cortex. The LIN-5–associated cortical dynein includes a relatively stable population, which, depending on PAR polarity, is enriched in the posterior, and thus may be critical for pulling forces.

Partial dynein perturbation reveals a contribution of dynein plus end tracking

Although dynein plus end tracking is not required for force generation and spindle positioning in WT conditions, it might function as a backup mechanism to ensure robust force generation. If so, a contribution of dynein plus end tracking may become detectable in certain stress conditions such as, for example, when dynein function is partially compromised. To examine this possibility, we used the temperature-sensitive (ts) allele *dhc-1(or195)*, which causes severe perturbation of DHC-1 function and 100% embryonic lethality at nonpermissive temperatures (Schmidt et al., 2005). We aimed to partially interfere with DHC-1 function at semipermissive temperatures to be able to examine whether *ebp-2* loss causes an enhanced or synthetic phenotype. Exposure of *dhc-1(or195)* mutants to temperatures ranging from 15 to 25°C revealed progressively more severe defects at higher temperatures (Fig. 7 A). The reduction in brood size and increase in embryonic lethality were strongly enhanced by the simultaneous presence of the *Δebp-2* allele at temperatures <25°C (Fig. 7 A). To assess whether this synergistic effect is related to spindle positioning, we performed spindle severing experiments with *dhc-1(or195)* and *dhc-1(or195); ebp-2(RNAi)* embryos, as homozygous *gfp::tbb-2; dhc-1(or195);* Δ*ebp-2* mutants were not viable. Most *dhc-1(or195); ebp-2(RNAi)* embryos could assemble functional mitotic spindles (100% for *gfp::tbb-2* and *gfp::tbb-2; ebp-2(RNAi)*, 87.5% for *gfp::tbb-2;*

of cortical MT contacts as mean MTs/μm² s^{-1} per embryo, and bars are means ± SEM. (F) Example images and quantifications of astral MT densities in control and *Δebp* mutant embryos, illustrated as radial intensity plots of fluorescent tubulin in metaphase (indicated in leftmost image). Plots were aligned and normalized to maximum values at the centrosome. *n* = 20 asters from 10 embryos per condition. Bars, 1 μm.

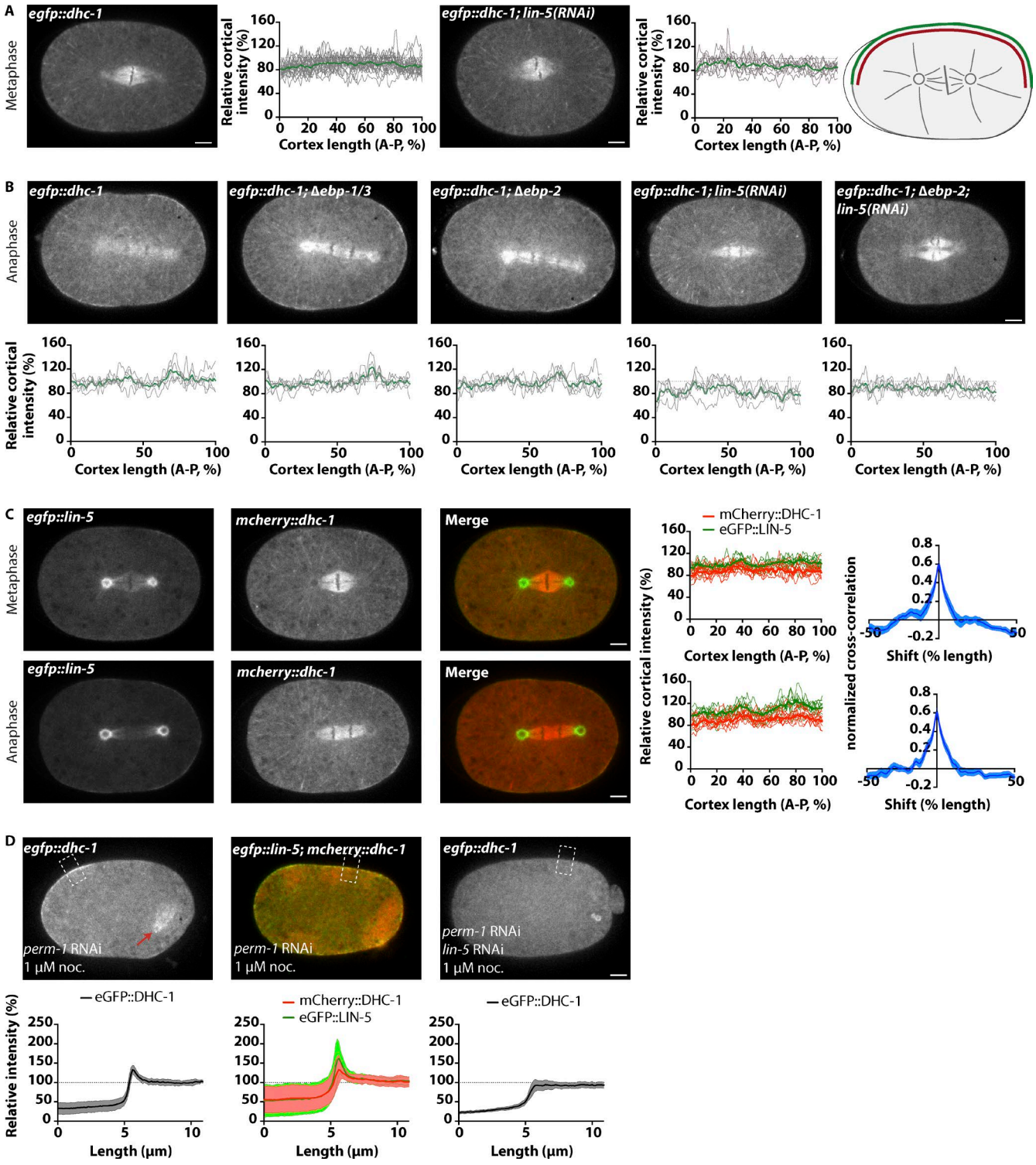

Figure 5. **Cortical dynein depends on recruitment from the cytoplasm by LIN-5 but not on EBP-2–mediated plus end tracking.** (A) SDCM images showing eGFP::DHC-1 localization in control and *lin-5(RNAi)* metaphase embryos. Graphs show relative cortical over cytoplasmic eGFP::DHC-1 intensities as measured along the cortex (far right, green line) and normalized to a cytoplasmic line (red). Dotted lines at y = 100% indicate a 1:1 cortex/cytoplasm ratio. Mean (green) and individual (gray) traces are shown. *n* = 12 embryos and 24 cortexes for control, and *n* = 5 embryos and 10 cortexes for *lin-5(RNAi)*. (B) SDCM images of anaphase embryos of indicated genotypes. Graphs show relative cortical over cytoplasmic eGFP::DHC-1 intensities, quantified and shown as described in A. *n* = 6 embryos per condition. (C) SDCM images show mCherry::DHC-1 and eGFP::LIN-5 localization. Mean (thick lines) and individual (thin lines) intensity plots are shown in left graphs. Right graphs show cross-correlation between cortical LIN-5 and DHC-1 plots expressed as means ± SEM. *n* = 10 embryos and 20 cortexes. (D) SDCM images showing dynein or LIN-5 localization in *perm-1(RNAi)* or *perm-1(RNAi); lin-5(RNAi)* embryos treated with 1 µM nocodazole (noc.). Graphs indicate fluorescence intensity profiles as measured in dashed boxes shown in superimposed panels. The red arrow points to mitotic spindle remnant. Plots are mean (*n* = 10) intensities relative to cytoplasmic values ± SD. Bars, 5 µm.

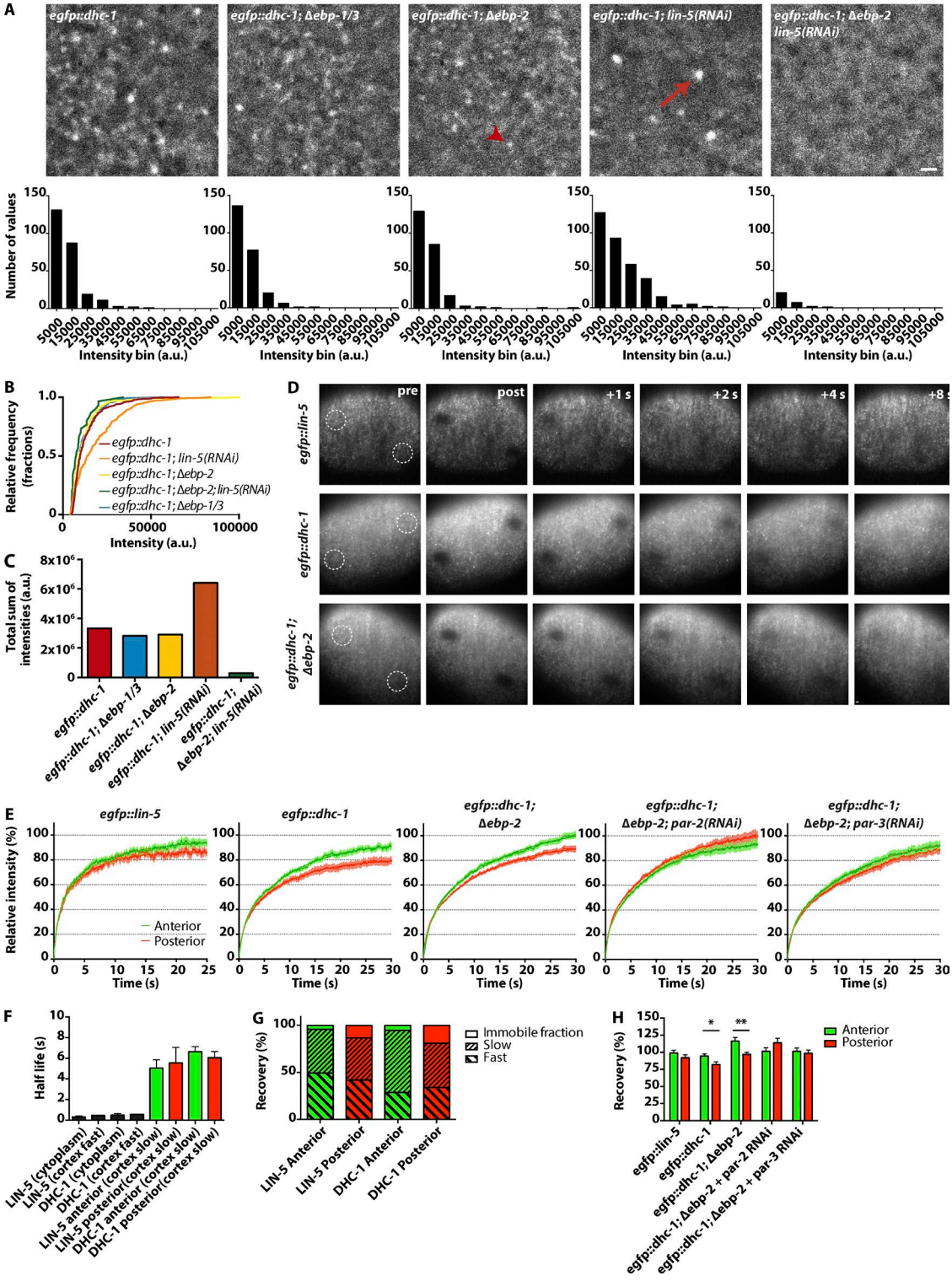

Figure 6. **Cortical dynein shows PAR polarity-dependent asymmetric dynamics in metaphase.** (A) TIRF images of early anaphase cortical eGFP::DHC-1 in different genetic backgrounds, showing plus end–associated (arrow) and cortical dynein dots (arrowhead). Bar graphs show frequency distributions of particle intensities from *n* = 6 embryos per condition during 10 s starting at posterior spindle displacement. Bar, 1 µm. (B) Cumulative frequency distribution of the data shown in A. (C) Comparison of total particle intensity sums (*n* = 30–344 particles) for each condition shown in A. (D) TIRF microscopy and FRAP of cortical eGFP::LIN-5 and eGFP::DHC-1 in anterior and posterior regions (indicated with dashed circles) during metaphase. (E) Quantification of FRAP as shown in D. Curves show means ± SEM. *egfp::lin-5*, *n* = 28 anterior and 22 posterior; *egfp::dhc-1* control, *n* = 19;, *Δebp-2*, *n* = 35; *Δebp-2; par-2(RNAi)*, *n* = 24; *Δebp-2; par-3(RNAi)*, *n* = 21. (F) Half-lives for cytoplasmic (one phase) and cortical (two phases: fast and slow) recovery curves. Bars represent means ± SEM. *egfp::lin-5* (cytoplasm), *n* = 7; *egfp::dhc-1* (cytoplasm), *n* = 30. *n* values for cortical FRAP curves are as in E. Unpaired Welch's Student's *t* test. (G) Quantification of the contribution of fast and slow phases of eGFP::LIN-5 and eGFP::DHC-1 to FRAP. *n* values are as in E. (H) Recovery of curves shown in E. *egfp::lin-5, egfp::dhc-1; Δebp-2, egfp::dhc-1; Δebp-2; par-2(RNAi)* anterior versus posterior. Wilcoxon matched-pairs signed rank test. *egfp::dhc-1; egfp::dhc-1;Δebp-2; par-3(RNAi)* anterior versus posterior. Paired Student's *t* test; *, P < 0.05; **, P < 0.01. *n* values are as in E.

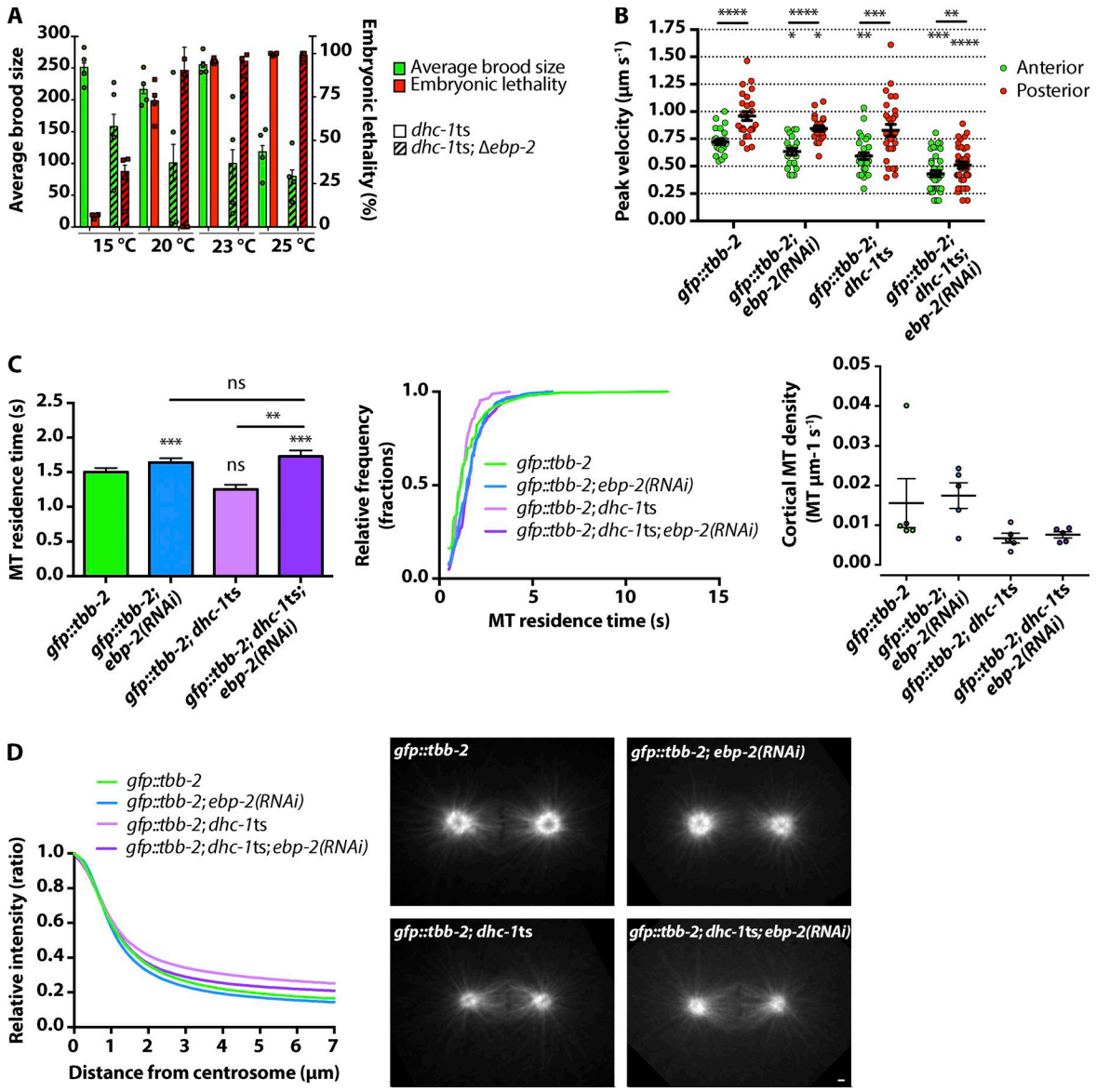

Figure 7. **EBP-2 is required for efficient force generation when dynein function is partially perturbed.** (A) Embryonic lethality and brood size of *dhc-1(or195*ts) and *dhc-1(or195*ts*); Δebp-2* strains at different temperatures shown as means ± SD. *n* = 4 animals each. (B) Quantification of centrosome velocities upon spindle severing. Bars show means ± SEM. Unpaired (between genotypes) and paired (within embryos) Student's *t* tests; **, P < 0.01; ***, P < 0.001; ****, P < 0.0001. *gfp::tbb-2* control, *n* = 25; *ebp-2(RNAi)*, *n* = 21; *dhc-1*ts, *n* = 28; *dhc-1*ts; *ebp-2(RNAi)*, *n* = 38. (C) Quantification of cortical MT residence time as described in Fig. 4 D. Bars are means ± SEM. Mann–Whitney *U* test; **, P < 0.01; ***, P < 0.001. *n* = 87–410 events from five embryos for each condition. Graphs show cumulative fractions of residence time distributions. Right graphs show density of cortical MT contacts as mean MTs/µm^2 s^{-1} per embryo, and bars are means ± SEM. (D) Quantification of astral MT densities in metaphase embryos measured as shown in Fig. 4 F. Plots were aligned and normalized to maximum values at the centrosome. *n* = 20 asters from 10 embryos per condition. Bar, 1 µm.

dhc-1(or195), and 73.3% for *gfp::tbb-2; dhc-1(or195); ebp-2(RNAi)* at 20°C). Interestingly, *ebp-2* RNAi strongly reduced pulling forces at the semipermissive temperature of 20°C (Fig. 7 B). This reduction did not result from an indirect effect on MT dynamics, as the *dhc-1(or195)* mutation itself did not significantly affect cortical MT residence time at 20°C or perturb the prolonged cortical contact caused by *ebp-2* RNAi (Fig. 7 C). Furthermore, although the density of astral MTs was reduced in the metaphase spindles of *dhc-1(or195)* embryos compared with WT, this mild effect was not further exacerbated by the knockdown of *ebp-2* (Fig. 7, C and D). Based on these results, we conclude that EBP-2–dependent plus end tracking of dynein contributes to robust spindle positioning and can serve as a backup mechanism that ensures efficient force generation when dynein function is partially perturbed.

Discussion

In this study, we investigated the localization and dynamics of the dynein complex during asymmetric spindle positioning in a well-established in vivo model, the *C. elegans* one-cell embryo. By tagging endogenous dynein and live imaging, we revealed two populations of dynein that together ensure robust cortical pulling force generation. To critically examine the importance of the MT plus end–bound dynein population, we generated

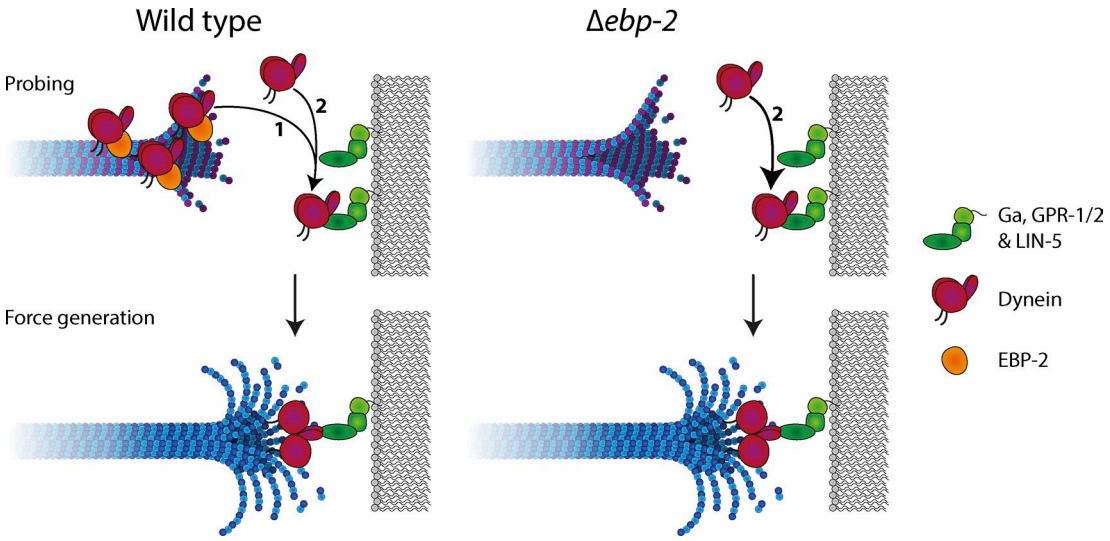

Figure 8. **Model.** Model of force generation in WT (left) and Δ*ebp-2* (right) situations as explained in the Discussion.

a complete knockout of all *ebp* family members and demonstrated that these genes are not essential but contribute to the control of MT dynamics and spindle formation. Finally, we provide a detailed analysis of the asymmetries and dynamics of the major FGC components dynein and LIN-5 at the cortex of one-cell embryos.

Although C-terminal tagging of the *dhc-1* dynein heavy chain was recently used (Zhang et al., 2015a), we observed that this creates partial loss of function. It is currently unclear whether this translates to dynein in other organisms. N- and C-terminally tagged yeast Dyn1 appear functional (Reck-Peterson et al., 2006). However, Dyn1 lacks the C-terminal regulatory extension present in the cytoplasmic dynein heavy chain of *C. elegans* and other organisms (Nicholas et al., 2015). A BAC transgene with a C-terminally GFP-tagged mouse dynein heavy chain is commonly used in mammalian studies (for example, see Poser et al., 2008). However, cells in culture with normal endogenous DHC do not depend on the tagged protein. Therefore, tagging the N-terminal DHC tail region instead of the C-terminal motor domain seems the best option for future in vivo studies.

Dynein plus end tracking was previously described for other organisms (Vaughan et al., 1999; Han et al., 2001; Lenz et al., 2006; Kobayashi and Murayama, 2009). In budding yeast, dynein is actively delivered to the cortex by a plus end tracking complex that also contains a kinesin (Lee et al., 2003; Sheeman et al., 2003; Markus and Lee, 2011). In animal cells, MT plus end–bound dynein is not transported by kinesins but is merely concentrated by binding to +TIPs, which are organized by EB proteins (Akhmanova and Steinmetz, 2015). Indeed, we found that loss of EBs completely abolished dynein plus end tracking. Strikingly, this mechanism, and in fact the whole EB protein family, turned out to be dispensable for *C. elegans* development and viability.

It is surprising that EBs are not essential in worms, because significant defects in MT dynamics and spindle formation or positioning have been reported in mammalian cells (Green et al., 2005; Draviam et al., 2006; Toyoshima and Nishida, 2007; Ban et al., 2009; Komarova et al., 2009; Xia et al., 2012; Ferreira et al., 2013). These studies did not report a block of cell division upon EB loss, and in fact, the phenotypes associated with EB knockouts in yeast and plants are relatively mild (Berlin et al., 1990; Bisgrove et al., 2008). Several considerations may explain the weak phenotypes. First, EB-dependent plus end tracking does not mediate transport and delivery of +TIPs but just promotes their transient concentration from the surrounding cytoplasm. This probably provides a limited gain over diffusion. Moreover, EB loss removes plus end recruitment of both positive and negative MT regulators. In addition, the phenotypes of constitutive knockouts might be milder than acute protein depletions because of compensatory mechanisms.

In contrast to EB-dependent plus end tracking, LIN-5 is essential for asymmetric spindle positioning. Using endogenously tagged LIN-5 and dynein, we observed that both proteins display a shallow cytoplasmic gradient throughout mitosis, reminiscent of the pattern described for GPR-1/2 and LIN-5 in fixed embryos (Park and Rose, 2008). Although the biological cause and function of this cytoplasmic asymmetry remains unknown, it indicates that cortical enrichment as judged by eye or cytoplasm-normalized plots can lead to its over- or underestimation. Thus, we compared nonnormalized cortical traces instead and found a strong correlation between LIN-5 and dynein cortical intensity patterns. Interestingly, our analysis did not reveal a clear A-P asymmetry in cortical localization for either protein at the time of initial spindle displacement in late metaphase. However, FRAP analysis combined with TIRF microscopy revealed an asymmetric and PAR-dependent stable population of dynein in the posterior. This subpopulation of LIN-5–bound dynein may be critical in force generation, as the number of active force generators has been reported to be higher in the posterior (Grill et al., 2003). LIN-5 showed only a small stable fraction at the cortex, which was nonsignificantly enriched in the posterior. We assume that not all cortical LIN-5 is dynein associated. Hence, the relevant population might be somewhat obscured in the total pool of cortical LIN-5. Collectively, our observations indicate that asymmetries in dynein behavior during initial spindle displacement probably do not result from asymmetric enrichment of LIN-5. Instead, other levels of control, such as protein phosphorylation and the Gα GTPase cycle, may determine LIN-5–dynein retention and pulling force asymmetry (Galli et al., 2011; Portegijs et al., 2016).

Dynein still localized to the cortex in embryos that lacked EBs or were treated with nocodazole. This strongly suggests that LIN-5 can recruit dynein directly from the cytoplasm as opposed to an MT-mediated delivery mechanism. MT-independent dynein recruitment has also been observed in nocodazole-treated mammalian cells; however, the correct cortical distribution of human dynein appears to depend on a dynamic astral MT network (Tame et al., 2014). Similarly, the localization of cortical dynein seemed randomized after nocodazole treatment of *C. elegans* embryos. Thus, in *C. elegans* and mammalian cells, MT-mediated delivery does not appear necessary for dynein localization to the cortex, but dynamic MTs appear to be required for the proper levels and distribution of dynein at the cortex.

We propose that dynein plus end tracking functions as a local enrichment mechanism (Fig. 8). By concentrating dynein at the plus end, MTs could promote local interaction of dynein with Gα–GPR-1/2–LIN-5 complexes at the cortex (Fig. 8, arrow 1). This hypothesis is supported by our finding that knockdown of EBP-2 enhances the reduction in forces caused by partial loss of DHC-1 function. In this context, enrichment of dynein at the plus end appears to be needed for efficient force generation. In the absence of EBs and thus dynein plus end tracking, FGCs would need to form through contacts between astral MTs and dynein-containing cortical complexes (Fig. 8, arrow 2). Although this single mechanism was thought to be less efficient (Ananthanarayanan et al., 2013), the prolonged cortical residence of MTs in the absence of EBP-2 might allow for successful probing of the cortex, which could explain why Δ*ebp-2* does not solely lead to reduced force generation. In WT cells, +TIPs form a protein-dense network, and the number of available binding sites in the vicinity of an MT plus end is limited (Duellberg et al., 2014). In EB-depleted cells, MT plus ends are probably less crowded, and cortical FGCs may associate with MTs more efficiently. Collectively, our work illustrates the complexity and robustness of the molecular mechanisms controlling the critical process of spindle positioning.

Materials and methods

C. elegans strains

A summary of the strains used in this study is included in Table S1. All strains were maintained at 20°C as described previously (Brenner, 1974) unless stated otherwise. Animals were grown on plates containing nematode growth medium seeded with OP50 *Escherichia coli* bacteria.

Generation of CRISPR/Cas9 repair templates and gRNAs

Homology arms of at least 1,500 bp flanking the CRISPR/Cas9 cleavage site were generated by PCR amplification from purified *C. elegans* genomic DNA using the KOD polymerase (Novagen). PCR products were inserted into the pBSK backbone by Gibson assembly (New England Biolabs, Inc.). For the generation of *ph::egfp::lov* and *egfp::dhc-1*, *egfp* was amplified from pMA-*egfp*, *ph* from P*wrt-2::gfp::ph* (Wildwater et al., 2011), and *lov* from *gfp::lovpep::unc-54UTR* (Harterink et al., 2016). For *mcherry::dhc-1* and *dhc-1::mcherry*, codon-optimized *mcherry* was amplified from TH0563-PAZ-*mcherry* (a gift from A. Hyman, Max Planck Institute of Molecular Cell Biology and Genetics, Dresden, Germany). Primers containing overlaps between PCR fragments, linker sequences encoding four glycine residues, and mutated gRNA sites were synthesized (Integrated DNA Technologies) and are listed in Table S3. For the generation of gRNA vectors, oligonucleotides were annealed and inserted into pJJR50 using T4 ligation (New England Biolabs, Inc.). Vectors were used to transform and were purified from DH5α-competent cells (QIAGEN).

CRISPR/Cas9-mediated genome editing

Injection of *C. elegans* adults in the germline was performed using an inverted microscope microinjection setup. Injection mixes contained a combination of 30–50 ng/µl P*eft-3::cas9* (46168; Addgene; Friedland et al., 2013), 50–100 ng/µl u6::sgRNA with sequences targeted against either *cxTi10816*, *dhc-1*, *ebp-1*, *ebp-2*, or *ebp-3*, 30–50 ng/µl of the repair template, 50 ng/µl PAGE-purified *pha-1* repair oligonucleotide (Integrated DNA technologies), 60 ng/µl pJW1285 (61252; Addgene; Ward, 2015), and 2.5 ng/µl P*myo-2::tdtomato* as a coinjection marker. Animals were grown for 3–5 d at either 20 or 25°C after injection, and transgenic progeny was selected based on either expression of tdTomato in the pharynx or survival at the nonpermissive temperature (25°C). Subsequent assessment of genome editing events was performed by either visual inspection using a widefield fluorescence microscope and/or PCR amplification using primers targeting the inserted FP and a genomic region situated outside of the range of homology arms, in case of *dhc-1*, or sequences flanking the predicted cut sites as well as an internal control, in case of the Δ*ebp-1/2/3* knockout mutants. The contexts of PCR-confirmed edited genomic loci were further inspected by sequencing (Macrogen Europe).

Quantification of embryonic lethality and total brood size

In three separate experiments, N2, SV1598, SV1619, and SV1803; N2, SV1868, SV1872, SV1877, and SV1882; or EU828 and SV1956 single L4-stage hermaphrodites were placed on OP50 feeding plates and kept at 15, 20, 23, and/or 25°C depending on the experiment. Animals were transferred to a new plate every day. On each plate, embryonic lethality was scored after 24 h, and brood size was scored 48 h after removal of the parent. Experiments were executed in quadruplicate.

Microscopy

For time-lapse imaging, embryos were dissected from *C. elegans* adults on coverslips in 0.8× egg salts buffer (94 mM NaCl, 32 mM KCl, 2.7 mM $CaCl_2$, 2.7 mM $MgCl_2$, and 4 mM Hepes, pH 7.5; Tagawa et al., 2001) and subsequently mounted on 4% agarose pads.

Live-cell SDCM imaging of one-cell embryos and HeLa cells was performed on an Eclipse T*i* with Perfect Focus System (Nikon), a CSU-X1-A1 spinning-disk confocal head (Yokogawa Electric Corporation), Plan Apochromat VC 60× 1.40 NA oil and S Fluor 100× 0.5–1.3 NA (at 1.3, for photoablation) objectives, an Evolve 512 electron-multiplying charge-coupled device camera (Photometrics), a DV2 two-channel beam-splitter for simultaneous dual-color imaging, Cobolt Calypso 491 nm (100 mW), Cobolt Jive 561 nm (100 mW), and Teem Photonics 355 nm Q-switched pulsed lasers controlled with the ILas system (Roper Scientific France/PICT-IBiSA, Institut Curie, used for photoablation), ET-GFP (49002), ET-mCherry (49008), and ET-GFP-mCherry (49022) filters, ASI motorized stage MS-2000-XYZ with Piezo Top Plate, and an LB10-3 filter wheel (Sutter Instrument). The microscope was controlled with MetaMorph 7.7 software and situated in a temperature-controlled room at 20°C.

HeLa cells were cultured as described previously (Splinter et al., 2012). For imaging of the dynein complex during mitosis, HeLa cells stably expressing DIC2-GFP were used. This cell line was generated and described previously in a BAC TransgeneOmics project (Poser et al., 2008). Imaging of mitotic cells was performed using the spinning-disk setup described in the previous paragraph, where the temperature was controlled at 37°C with a Tokai Hit INUBG2E-ZILCS Stage Top Incubator during experiments.

For regular single- and dual-color channel imaging experiments, images were acquired in either streaming mode with 50, 100, 250, 500, or 1,000 ms exposure or time-lapse mode with 500 ms exposure and 5-s intervals. Laser power was kept constant within experiments. For spindle bisection assays, spindles were imaged after photoablation in streaming mode with 500 ms exposure time.

Simultaneous dual-color TIRF imaging of embryos was performed on an Eclipse T*i* with Perfect Focus System, an Apochromat TIRF 100× 1.49 NA oil objective (Nikon), an Evolve 512 electron-multiplying charge-coupled device camera, an Optosplit III beam-splitter (Andor Technology) for simultaneous dual-color imaging, 488-nm (150 mW) and Cobolt Jive 561-nm (100 mW) lasers, ET-GFP (49002), ET-mCherry (49008), and ET-GFPmCherry (49022) filters, an ASI motorized stage MS-2000-XY System for Inverted Microscope Te/Ti 2000 (Nikon), and an LB10-3 filter wheel. Acquisition was controlled with MetaMorph 7.7 software (Molecular Devices), and the setup was situated in a temperature-controlled room at 20°C.

Single-color TIRF imaging of embryos was performed on either the above-mentioned TIRF setup or on an identical TIRF setup in which lasers were controlled by the Ilas-2 system (Roper Scientific), and image acquisition was controlled with MetaMorph 7.8 software (Molecular Devices).

Live-cell widefield time-lapse DIC microscopy imaging of embryos was performed on an Axioplan upright microscope with a 100× 1.4 NA Plan Apochromat objective controlled by AxioVision Rel 4.7 software (ZEISS) at an acquisition rate of one image per 2 s with constant exposure time and light intensity. Embryos were followed from pronuclear meeting until completion of the first cell division.

Images acquired by SDCM and TIRF microscopy were prepared for publication in ImageJ (National Institutes of Health) by linear adjustment of brightness and contrast, subtraction of background intensity as measured in images outside cells, and frame averaging. For images in Figs. 2, 4 D, 6 A, and S2 (A and B), a Gaussian blur filter was applied for background subtraction using ImageJ. Fluorophores used in this study to visualize proteins of interest include eGFP, mCherry, and YFP.

RNA-mediated interference

For feeding RNAi experiments (Timmons and Fire, 1998), L4 animals were grown on seeded RNAi plates for 24 h at 20°C or 48 h at 15°C before imaging sessions (*lin-5*, *ebp-1/3*, *ebp-2*, and *gpr-1*). Alternatively, the gonads of young adults were injected with double-stranded RNA targeting RNA molecules of interest (*perm-1* and *perm-1* + *lin-5*) and grown for 20 h at 15°C (Fire et al., 1998). For these experiments, the products of T7 PCRs on RNAi clones were used as templates for in vitro double-stranded RNA synthesis using the MEGAscript T7 transcription kit (Thermo Fisher Scientific). Clones from both the Vidal and Ahringer RNAi libraries were used (Kamath et al., 2003; Rual et al., 2004).

UV laser spindle midzone severing

Severing of the mitotic spindle was performed in essence as described previously (Grill et al., 2001; Portegijs et al., 2016). AZ224, TH65, SV893, SV1874, SV1879, and SV1900 one-cell embryos were imaged during mitosis at 20°C using a spinning-disk confocal microscope equipped with a Teem Photonics 355-nm Q-switched pulsed laser controlled with the ILas system. At anaphase onset, as judged by spindle morphology visualized with GFP::TBB-2 or TBA-2::YFP, embryos were subjected to spindle bisection as shown in Fig. 4 B and Video 9. Subsequent displacement of centrosomes was followed by stream acquisition with 500-ms exposure time. Centrosome peak velocities after spindle severing were subsequently tracked automatically using the FIJI TrackMate plugin (ImageJ).

FRAP

Local photobleaching of eGFP::LIN-5 and eGFP::DHC-1 fluorescence signal was performed during metaphase in a circular region with a diameter of 45 px (~2.8 µm) in both the anterior and posterior cortex (except for cytoplasmic LIN-5 FRAP experiments, which were performed only in the anterior), and recovery was followed for up to 30 s afterward. Intensities within the photobleached regions and a background area outside the signal of the embryo cortex were measured using a circular region with a diameter of 54 px (~3.38 µm), and a bleaching control was taken between but not overlapping the anterior and posterior photobleached regions. Recovery of the fluorescent signals was set to 100% based on the mean intensity from 20 frames (1 s) before bleaching in the same region and was set to 0% directly after. All values were normalized to account for camera background and acquisition photobleaching as described previously (Phair et al., 2003). Recovery curves of cortical FRAP experiments were aligned at their minimum value and fitted using one- and two-phase nonlinear regression analysis in Prism 6 (GraphPad Software). For unpaired statistical comparison with initial phase parameters of cortical FRAP fits, individual cytoplasmic recovery parameters were approached by one-phase nonlinear regression analysis and subsequently averaged and tested for significance. For paired statistical testing of plateau values from cortical FRAP curves, individual curves were fit by one-phase nonlinear regression analysis, and anterior and posterior parameters were subsequently compared within samples.

Drug treatment of early embryos

To allow for small molecule drugs to enter the early *C. elegans* embryo, L4 animals were treated with *perm-1* RNAi for 20 h before experiments (Carvalho et al., 2011). Egg-laying SV1803 or SV1635 adults were then splayed onto coverslips in 0.8× egg salts buffer with 1 µM nocodazole and mounted on slides with a concave indentation, which prevents compression of the embryos. Metaphase one-cell embryos were identified by the presence of polar bodies, enlarged centrosomes, a spindle remnant, and absence of a nuclear envelope, and then they were imaged by SDCM (Portegijs et al., 2016).

Data analysis

All intensity profile measurements of SDCM and TIRF microscopy data were generated using ImageJ and FIJI.

For cortical intensity profiles of strains SV1589, SV1619, SV1635, and SV1803, both halves of each embryo were traced with a 5-px-wide freehand line from the anterior to the posterior pole with five replicates, and five matching traces were generated below each cortex in the cytoplasm. Intensity profiles were background corrected, and each group of five traces was then averaged and subsequently divided into 100 bins to correct for varying lengths of the plots. Cortical plots were then plotted either with or without normalization over corresponding cytoplasmic measurements or the mean thereof.

Analysis of the timing of key mitotic events and position of the nucleocentrosomal complex and centrosomes from DIC videos of N2, SV1868, SV1872, SV1877, and SV1882 strains was performed by hand using ImageJ.

Quantifications of cortical MT residence time were performed automatically by use of the FIJI plugin TrackMate v3.4.2 at 6 px estimated blob diameter and a threshold value of 1,500. TIRF microscopy videos from strains AZ244, SV1874, TH65, SV1879, SV1900, and SV893 starting at posterior spindle displacement with 20 s total duration were background corrected by application of a Gaussian blur filter before analysis. Detected spots were then filtered to contain only those with <10 px displacement, which excludes any laterally growing MTs from the analysis.

Speeds of EBP-2::GFP and mCherry::DHC-1 comets in strain SV1857 as imaged by SDCM during metaphase were calculated based on angles made by tracks in kymograph images generated in ImageJ with the KymoResliceWide plugin. Kymograph locations were manually selected between the centrosome and cell cortex.

Quantification of the colocalization between EBP-2::GFP and mCherry::DHC-1 comets in strain SV1857 as imaged by simultaneous dual-color TIRF microscopy was executed using the ComDet plugin v0.3.6, and the same dual-color images with one channel inverted horizontally were used as an internal control. Particles were detected in both green and red channels independently at approximated particle sizes of 4 (red) and 4.5 (green) px with sensitivities of signal/noise ratio equaling 4 and 5, respectively. Colocalization was determined based on a maximum distance of 8.00 px.

Automatic tracking of particle intensities in TIRF videos of SV1803, SV1874, and SV1879 was executed using the ImageJ Analyze Particles plugin with parameter size = 10–∞ px, circularity = 0.10–1.00, and with exclusion of particles on edges after background-subtraction and manual image thresholding.

Radial intensity profiles of astral MT networks were generated using the Radial Profile Angle plugin for ImageJ, set to measure intensities in a 180° angle around each of two centrosomes with a radius of 150 px in metaphase embryos. Intensity profiles were then aligned at their maximum values corresponding with the outer rim of the centrosome and normalized to their maximum values.

Cross-correlation analysis was performed on averaged nonnormalized cortical intensity profiles of strain SV1635 using a custom MATLAB (MathWorks) script and the following equation, which calculates the normalized cross-correlation for each Δx shift of one channel with respect to another:

$$\gamma(\Delta x) = \frac{\sum_x \left[I_1(x) - \langle I_1 \rangle\right]\left[I_2(x-\Delta x) - \langle I_2 \rangle\right]}{\sqrt{\sum_x \left[I_1(x) - \langle I_1 \rangle\right]^2 \sum_x \left[I_2(x-\Delta x) - \langle I_2 \rangle\right]^2}}.$$

All numerical data processing and graph generation was performed using Excel 2011 (Microsoft) and Prism 6.

Statistical analysis

All data are expressed as means with either SD or SEM as indicated in the legends of each figure. Statistical differences were determined using two-tailed paired and unpaired Student's *t* tests, Mann–Whitney *U* tests, and the Wilcoxon matched-pairs signed rank test. Before selection of appropriate statistical analyses, datasets were tested for a Gaussian distribution using the D'Agostino-Pearson omnibus K2 normality test. A p-value of <0.05 was considered to be significant. *, $P < 0.05$; **, $P < 0.01$; ***, $P < 0.001$; ****, $P < 0.0001$. All statistical analyses were performed using Prism 6.

Online supplemental material

Fig. S1 shows dynein plus end tracking in cell types other than the one-cell *C. elegans* embryo. Fig. S2 shows the localization of dynein at the mitotic spindle and its colocalization with dynactin at the MT plus end. Fig. S3 contains quantifications of various mitotic events and their timing as visualized by DIC microscopy as in Fig. 3 E. Fig. S4 shows that EBP-2 is required for assembly of the spindle midzone and that cortical dynein patches follow the oscillatory behavior of the anaphase spindle. Fig. S5 contains extended analyses of the subcellular localization patterns of LIN-5 and DHC-1 shown in Fig. 5 C as well as recovery curves for the cytoplasmic FRAP experiments quantified in Fig. 6 (F and H). Table S1 contains a list of the *C. elegans* strains used in this study. Table S2 contains parameters from nonlinear regression curve fits of eGFP::LIN-5 and eGFP::DHC-1 FRAP experiments. Table S3 contains a list of the primers used in this study for CRISPR/Cas9-assisted genome engineering. Video 1 shows overlap of mCherry::DHC-1 with GFP::TBB-2 as in Fig. 2 A. Video 2 shows colocalization of mCherry::DHC-1 with EBP-2::GFP as in Fig. 2 B. Video 3 shows cortical overlap of mCherry::DHC-1 with GFP::TBB-2 as in Fig. 2 E. Video 4 shows cortical overlap of mCherry::DHC-1 with EBP-2::GFP as in Fig. 2 F. Video 5 shows co-occurrence of dynein comets reaching the cortex and the formation of membrane invaginations as in Fig. 2 H. Video 6 shows the localization of eGFP::DHC-1 in Δ*ebp* mutants as in Fig. 3 C. Video 7 shows DIC videos of mitotic WT and Δ*ebp* one-cell embryos as in Fig. 3 E. Video 8 shows the genetic dissection of two cortical dynein populations as in Fig. 6 A. Video 9 shows an example of UV laser-mediated spindle severing as in Fig. 4 B. Video 10 shows end-on MT–cortex contacts as visualized by TIRF microscopy as shown in Fig. 4 D.

Acknowledgments

We thank all members of the van den Heuvel, Akhmanova, and Boxem groups for helpful discussions and support. We acknowledge Wormbase and the Biology Imaging Center at the Faculty of Sciences, Department of Biology, Utrecht University. Some strains were provided by the Caenorhabditis Genetics Center funded by National Institutes of Health Office of Research Infrastructure Programs (P40 OD010440).

This work was supported by a European Research Council Synergy grant 609822 to A. Akhmanova and is part of the Netherlands Organization for Scientific Research program CW711.011.01 (to S. van den Heuvel).

The authors declare no competing financial interests.

Author contributions: A. Akhmanova, R. Schmidt, and S. van den Heuvel designed the study, analyzed the data, and wrote the paper. R. Schmidt carried out most experiments, L.-E. Fielmich performed the LIN-5 knock in and FRAP studies, I. Grigoriev was responsible for the analysis of HeLa cells and, with E.A. Katrukha, provided technical support of microscopy, and E.A. Katrukha supported data analysis.

Submitted: 11 July 2016
Revised: 8 May 2017
Accepted: 28 June 2017

References

Akhmanova, A., and M.O. Steinmetz. 2015. Control of microtubule organization and dynamics: two ends in the limelight. *Nat. Rev. Mol. Cell Biol.* 16:711–726. http://dx.doi.org/10.1038/nrm4084

Ananthanarayanan, V., M. Schattat, S.K. Vogel, A. Krull, N. Pavin, and I.M. Tolić-Nørrelykke. 2013. Dynein motion switches from diffusive to directed upon cortical anchoring. *Cell.* 153:1526–1536. http://dx.doi.org/10.1016/j.cell.2013.05.020

Ban, R., H. Matsuzaki, T. Akashi, G. Sakashita, H. Taniguchi, S.Y. Park, H. Tanaka, K. Furukawa, and T. Urano. 2009. Mitotic regulation of the stability of microtubule plus-end tracking protein EB3 by ubiquitin ligase SIAH-1 and Aurora mitotic kinases. *J. Biol. Chem.* 284:28367–28381. http://dx.doi.org/10.1074/jbc.M109.000273

Berends, C.W.H., J. Muñoz, V. Portegijs, R. Schmidt, I. Grigoriev, M. Boxem, A. Akhmanova, A.J.R. Heck, and S. van den Heuvel. 2013. F-actin asymmetry and the endoplasmic reticulum-associated TCC-1 protein contribute to stereotypic spindle movements in the *Caenorhabditis elegans* embryo. *Mol. Biol. Cell.* 24:2201–2215. http://dx.doi.org/10.1091/mbc.E13-02-0076

Berlin, V., C.A. Styles, and G.R. Fink. 1990. BIK1, a protein required for microtubule function during mating and mitosis in Saccharomyces cerevisiae, colocalizes with tubulin. *J. Cell Biol.* 111:2573–2586. http://dx.doi.org/10.1083/jcb.111.6.2573

Berrueta, L., J.S. Tirnauer, S.C. Schuyler, D. Pellman, and B.E. Bierer. 1999. The APC-associated protein EB1 associates with components of the dynactin complex and cytoplasmic dynein intermediate chain. *Curr. Biol.* 9:425–428. http://dx.doi.org/10.1016/S0960-9822(99)80190-0

Bieling, P., L. Laan, H. Schek, E.L. Munteanu, L. Sandblad, M. Dogterom, D. Brunner, and T. Surrey. 2007. Reconstitution of a microtubule plus-end tracking system in vitro. *Nature.* 450:1100–1105. http://dx.doi.org/10.1038/nature06386

Bisgrove, S.R., Y.-R.J. Lee, B. Liu, N.T. Peters, and D.L. Kropf. 2008. The microtubule plus-end binding protein EB1 functions in root responses to touch and gravity signals in *Arabidopsis*. *Plant Cell.* 20:396–410. http://dx.doi.org/10.1105/tpc.107.056846

Brenner, S. 1974. The genetics of *Caenorhabditis elegans*. *Genetics.* 77:71–94.

Carvalho, A., S.K. Olson, E. Gutierrez, K. Zhang, L.B. Noble, E. Zanin, A. Desai, A. Groisman, and K. Oegema. 2011. Acute drug treatment in the early *C. elegans* embryo. *PLoS One.* 6:e24656. http://dx.doi.org/10.1371/journal.pone.0024656

Colombo, K., S.W. Grill, R.J. Kimple, F.S. Willard, D.P. Siderovski, and P. Gönczy. 2003. Translation of polarity cues into asymmetric spindle positioning in *Caenorhabditis elegans* embryos. *Science.* 300:1957–1961. http://dx.doi.org/10.1126/science.1084146

Draviam, V.M., I. Shapiro, B. Aldridge, and P.K. Sorger. 2006. Misorientation and reduced stretching of aligned sister kinetochores promote chromosome missegregation in EB1- or APC-depleted cells. *EMBO J.* 25:2814–2827. http://dx.doi.org/10.1038/sj.emboj.7601168

Duellberg, C., M. Trokter, R. Jha, I. Sen, M.O. Steinmetz, and T. Surrey. 2014. Reconstitution of a hierarchical +TIP interaction network controlling microtubule end tracking of dynein. *Nat. Cell Biol.* 16:804–811. http://dx.doi.org/10.1038/ncb2999

Ferreira, J.G., A.J. Pereira, A. Akhmanova, and H. Maiato. 2013. Aurora B spatially regulates EB3 phosphorylation to coordinate daughter cell adhesion with cytokinesis. *J. Cell Biol.* 201:709–724. http://dx.doi.org/10.1083/jcb.201301131

Fire, A., S. Xu, M.K. Montgomery, S.A. Kostas, S.E. Driver, and C.C. Mello. 1998. Potent and specific genetic interference by double-stranded RNA in *Caenorhabditis elegans*. *Nature.* 391:806–811. http://dx.doi.org/10.1038/35888

Friedland, A.E., Y.B. Tzur, K.M. Esvelt, M.P. Colaiácovo, G.M. Church, and J.A. Calarco. 2013. Heritable genome editing in *C. elegans* via a CRISPR-Cas9 system. *Nat. Methods.* 10:741–743. http://dx.doi.org/10.1038/nmeth.2532

Galli, M., and S. van den Heuvel. 2008. Determination of the cleavage plane in early *C. elegans* embryos. *Annu. Rev. Genet.* 42:389–411. http://dx.doi.org/10.1146/annurev.genet.40.110405.090523

Galli, M., J. Muñoz, V. Portegijs, M. Boxem, S.W. Grill, A.J.R. Heck, and S. van den Heuvel. 2011. aPKC phosphorylates NuMA-related LIN-5 to position the mitotic spindle during asymmetric division. *Nat. Cell Biol.* 13:1132–1138. http://dx.doi.org/10.1038/ncb2315

Gassmann, R., A. Essex, J.-S. Hu, P.S. Maddox, F. Motegi, A. Sugimoto, S.M. O'Rourke, B. Bowerman, I. McLeod, J.R. Yates III, et al. 2008. A new mechanism controlling kinetochore–microtubule interactions revealed by comparison of two dynein-targeting components: SPDL-1 and the Rod/Zwilch/Zw10 complex. *Genes Dev.* 22:2385–2399. http://dx.doi.org/10.1101/gad.1687508

Gotta, M., and J. Ahringer. 2001. Distinct roles for Gα and Gβγ in regulating spindle position and orientation in *Caenorhabditis elegans* embryos. *Nat. Cell Biol.* 3:297–300. http://dx.doi.org/10.1038/35060092

Gotta, M., Y. Dong, Y.K. Peterson, S.M. Lanier, and J. Ahringer. 2003. Asymmetrically distributed *C. elegans* homologs of AGS3/PINS control spindle position in the early embryo. *Curr. Biol.* 13:1029–1037. http://dx.doi.org/10.1016/S0960-9822(03)00371-3

Green, R.A., R. Wollman, and K.B. Kaplan. 2005. APC and EB1 function together in mitosis to regulate spindle dynamics and chromosome alignment. *Mol. Biol. Cell.* 16:4609–4622. http://dx.doi.org/10.1091/mbc.E05-03-0259

Grill, S.W., P. Gönczy, E.H. Stelzer, and A.A. Hyman. 2001. Polarity controls forces governing asymmetric spindle positioning in the *Caenorhabditis elegans* embryo. *Nature.* 409:630–633. http://dx.doi.org/10.1038/35054572

Grill, S.W., J. Howard, E. Schäffer, E.H.K. Stelzer, and A.A. Hyman. 2003. The distribution of active force generators controls mitotic spindle position. *Science.* 301:518–521. http://dx.doi.org/10.1126/science.1086560

Gusnowski, E.M., and M. Srayko. 2011. Visualization of dynein-dependent microtubule gliding at the cell cortex: implications for spindle positioning. *J. Cell Biol.* 194:377–386. http://dx.doi.org/10.1083/jcb.201103128

Han, G., B. Liu, J. Zhang, W. Zuo, N.R. Morris, and X. Xiang. 2001. The *Aspergillus* cytoplasmic dynein heavy chain and NUDF localize to microtubule ends and affect microtubule dynamics. *Curr. Biol.* 11:719–724. http://dx.doi.org/10.1016/S0960-9822(01)00200-7

Harterink, M., P. van Bergeijk, C. Allier, B. de Haan, S. van den Heuvel, C.C. Hoogenraad, and L.C. Kapitein. 2016. Light-controlled intracellular transport in *Caenorhabditis elegans*. *Curr. Biol.* 26:R153–R154. http://dx.doi.org/10.1016/j.cub.2015.12.016

Hendricks, A.G., J.E. Lazarus, E. Perlson, M.K. Gardner, D.J. Odde, Y.E. Goldman, and E.L.F. Holzbaur. 2012. Dynein tethers and stabilizes dynamic microtubule plus ends. *Curr. Biol.* 22:632–637. http://dx.doi.org/10.1016/j.cub.2012.02.023

Honnappa, S., O. Okhrimenko, R. Jaussi, H. Jawhari, I. Jelesarov, F.K. Winkler, and M.O. Steinmetz. 2006. Key interaction modes of dynamic +TIP networks. *Mol. Cell.* 23:663–671. http://dx.doi.org/10.1016/j.molcel.2006.07.013

Kamath, R.S., A.G. Fraser, Y. Dong, G. Poulin, R. Durbin, M. Gotta, A. Kanapin, N. Le Bot, S. Moreno, M. Sohrmann, et al. 2003. Systematic functional analysis of the *Caenorhabditis elegans* genome using RNAi. *Nature.* 421:231–237. http://dx.doi.org/10.1038/nature01278

Kardon, J.R., and R.D. Vale. 2009. Regulators of the cytoplasmic dynein motor. *Nat. Rev. Mol. Cell Biol.* 10:854–865. http://dx.doi.org/10.1038/nrm2804

Kimura, K., and A. Kimura. 2011. Intracellular organelles mediate cytoplasmic pulling force for centrosome centration in the *Caenorhabditis elegans* early embryo. *Proc. Natl. Acad. Sci. USA.* 108:137–142. http://dx.doi.org/10.1073/pnas.1013275108

Kirschner, M., and T. Mitchison. 1986. Beyond self-assembly: From microtubules to morphogenesis. *Cell.* 45:329–342. http://dx.doi.org/10.1016/0092-8674(86)90318-1

Kiyomitsu, T., and I.M. Cheeseman. 2012. Chromosome- and spindle-pole-derived signals generate an intrinsic code for spindle position and orientation. *Nat. Cell Biol.* 14:311–317. http://dx.doi.org/10.1038/ncb2440

Kobayashi, T., and T. Murayama. 2009. Cell cycle-dependent microtubule-based dynamic transport of cytoplasmic dynein in mammalian cells. *PLoS One.* 4:e7827. http://dx.doi.org/10.1371/journal.pone.0007827

Komarova, Y., C.O. De Groot, I. Grigoriev, S.M. Gouveia, E.L. Munteanu, J.M. Schober, S. Honnappa, R.M. Buey, C.C. Hoogenraad, M. Dogterom, et al. 2009. Mammalian end binding proteins control persistent microtubule growth. *J. Cell Biol.* 184:691–706. http://dx.doi.org/10.1083/jcb.200807179

Kotak, S., C. Busso, and P. Gönczy. 2012. Cortical dynein is critical for proper spindle positioning in human cells. *J. Cell Biol.* 199:97–110. http://dx.doi.org/10.1083/jcb.201203166

Kozlowski, C., M. Srayko, and F. Nedelec. 2007. Cortical microtubule contacts position the spindle in *C. elegans* embryos. *Cell.* 129:499–510. http://dx.doi.org/10.1016/j.cell.2007.03.027

Laan, L., N. Pavin, J. Husson, G. Romet-Lemonne, M. van Duijn, M.P. López, R.D. Vale, F. Jülicher, S.L. Reck-Peterson, and M. Dogterom. 2012. Cortical dynein controls microtubule dynamics to generate pulling forces that position microtubule asters. *Cell.* 148:502–514. http://dx.doi.org/10.1016/j.cell.2012.01.007

Lansbergen, G., Y. Komarova, M. Modesti, C. Wyman, C.C. Hoogenraad, H.V. Goodson, R.P. Lemaitre, D.N. Drechsel, E. van Munster, T.W.J. Gadella Jr., et al. 2004. Conformational changes in CLIP-170 regulate its binding to microtubules and dynactin localization. *J. Cell Biol.* 166:1003–1014. http://dx.doi.org/10.1083/jcb.200402082

Lee, W.L., J.R. Oberle, and J.A. Cooper. 2003. The role of the lissencephaly protein Pac1 during nuclear migration in budding yeast. *J. Cell Biol.* 160:355–364. http://dx.doi.org/10.1083/jcb.200209022

Lenz, J.H., I. Schuchardt, A. Straube, and G. Steinberg. 2006. A dynein loading zone for retrograde endosome motility at microtubule plus-ends. *EMBO J.* 25:2275–2286. http://dx.doi.org/10.1038/sj.emboj.7601119

Lorson, M.A., H.R. Horvitz, and S. van den Heuvel. 2000. LIN-5 is a novel component of the spindle apparatus required for chromosome segregation and cleavage plane specification in *Caenorhabditis elegans*. *J. Cell Biol.* 148:73–86. http://dx.doi.org/10.1083/jcb.148.1.73

Markus, S.M., and W.L. Lee. 2011. Regulated offloading of cytoplasmic dynein from microtubule plus ends to the cortex. *Dev. Cell.* 20:639–651. http://dx.doi.org/10.1016/j.devcel.2011.04.011

Maurer, S.P., F.J. Fourniol, G. Bohner, C.A. Moores, and T. Surrey. 2012. EBs recognize a nucleotide-dependent structural cap at growing microtubule ends. *Cell.* 149:371–382. http://dx.doi.org/10.1016/j.cell.2012.02.049

Maurer, S.P., N.I. Cade, G. Bohner, N. Gustafsson, E. Boutant, and T. Surrey. 2014. EB1 accelerates two conformational transitions important for microtubule maturation and dynamics. *Curr. Biol.* 24:372–384. http://dx.doi.org/10.1016/j.cub.2013.12.042

Morin, X., and Y. Bellaïche. 2011. Mitotic spindle orientation in asymmetric and symmetric cell divisions during animal development. *Dev. Cell.* 21:102–119. http://dx.doi.org/10.1016/j.devcel.2011.06.012

Nguyen-Ngoc, T., K. Afshar, and P. Gönczy. 2007. Coupling of cortical dynein and Gα proteins mediates spindle positioning in *Caenorhabditis elegans*. *Nat. Cell Biol.* 9:1294–1302. http://dx.doi.org/10.1038/ncb1649

Nicholas, M.P., P. Höök, S. Brenner, C.L. Wynne, R.B. Vallee, and A. Gennerich. 2015. Control of cytoplasmic dynein force production and processivity by its C-terminal domain. *Nat. Commun.* 6:6206. http://dx.doi.org/10.1038/ncomms7206

Park, D.H., and L.S. Rose. 2008. Dynamic localization of LIN-5 and GPR-1/2 to cortical force generation domains during spindle positioning. *Dev. Biol.* 315:42–54. http://dx.doi.org/10.1016/j.ydbio.2007.11.037

Pecreaux, J., J.-C. Röper, K. Kruse, F. Jülicher, A.A. Hyman, S.W. Grill, and J. Howard. 2006. Spindle oscillations during asymmetric cell division require a threshold number of active cortical force generators. *Curr. Biol.* 16:2111–2122. http://dx.doi.org/10.1016/j.cub.2006.09.030

Phair, R.D., S.A. Gorski, and T. Misteli. 2003. Measurement of dynamic protein binding to chromatin in vivo, using photobleaching microscopy. *Methods Enzymol.* 375:393–414. http://dx.doi.org/10.1016/S0076-6879(03)75025-3

Portegijs, V., L.-E. Fielmich, M. Galli, R. Schmidt, J. Muñoz, T. van Mourik, A. Akhmanova, A.J.R. Heck, M. Boxem, and S. van den Heuvel. 2016. Multisite phosphorylation of NuMA-related LIN-5 controls mitotic spindle positioning in *C. elegans*. *PLoS Genet.* 12:e1006291. http://dx.doi.org/10.1371/journal.pgen.1006291

Poser, I., M. Sarov, J.R.A. Hutchins, J.-K. Hériché, Y. Toyoda, A. Pozniakovsky, D. Weigl, A. Nitzsche, B. Hegemann, A.W. Bird, et al. 2008. BAC TransgeneOmics: a high-throughput method for exploration of protein function in mammals. *Nat. Methods.* 5:409–415. http://dx.doi.org/10.1038/nmeth.1199

Praitis, V., E. Casey, D. Collar, and J. Austin. 2001. Creation of low-copy integrated transgenic lines in *Caenorhabditis elegans*. *Genetics.* 157:1217–1226.

Reck-Peterson, S.L., A. Yildiz, A.P. Carter, A. Gennerich, N. Zhang, and R.D. Vale. 2006. Single-molecule analysis of dynein processivity and stepping behavior. *Cell.* 126:335–348. http://dx.doi.org/10.1016/j.cell.2006.05.046

Redemann, S., J. Pecreaux, N.W. Goehring, K. Khairy, E.H.K. Stelzer, A.A. Hyman, and J. Howard. 2010. Membrane invaginations reveal cortical sites that pull on mitotic spindles in one-cell *C. elegans* embryos. *PLoS One.* 5:e12301. http://dx.doi.org/10.1371/journal.pone.0012301

Rose, L., and P. Gönczy. 2014. Polarity establishment, asymmetric division and segregation of fate determinants in early *C. elegans* embryos. *WormBook.* http://dx.doi.org/10.1895/wormbook.1.30.2

Rual, J.F., J. Ceron, J. Koreth, T. Hao, A.S. Nicot, T. Hirozane-Kishikawa, J. Vandenhaute, S.H. Orkin, D.E. Hill, S. van den Heuvel, and M. Vidal. 2004. Toward improving *Caenorhabditis elegans* phenome mapping with an ORFeome-based RNAi library. *Genome Res.* 14(10b, 10B):2162–2168. http://dx.doi.org/10.1101/gr.2505604

Schmidt, D.J., D.J. Rose, W.M. Saxton, and S. Strome. 2005. Functional analysis of cytoplasmic dynein heavy chain in *Caenorhabditis elegans* with fast-acting temperature-sensitive mutations. *Mol. Biol. Cell.* 16:1200–1212. http://dx.doi.org/10.1091/mbc.E04-06-0523

Sheeman, B., P. Carvalho, I. Sagot, J. Geiser, D. Kho, M.A. Hoyt, and D. Pellman. 2003. Determinants of *S. cerevisiae* dynein localization and activation: Implications for the mechanism of spindle positioning. *Curr. Biol.* 13:364–372. http://dx.doi.org/10.1016/S0960-9822(03)00013-7

Slep, K.C., and R.D. Vale. 2007. Structural basis of microtubule plus end tracking by XMAP215, CLIP-170, and EB1. *Mol. Cell.* 27:976–991. http://dx.doi.org/10.1016/j.molcel.2007.07.023

Splinter, D., D.S. Razafsky, M.A. Schlager, A. Serra-Marques, I. Grigoriev, J. Demmers, N. Keijzer, K. Jiang, I. Poser, A.A. Hyman, et al. 2012. BICD2, dynactin, and LIS1 cooperate in regulating dynein recruitment to cellular structures. *Mol. Biol. Cell.* 23:4226–4241. http://dx.doi.org/10.1091/mbc.E12-03-0210

Srayko, M., A. Kaya, J. Stamford, and A.A. Hyman. 2005. Identification and characterization of factors required for microtubule growth and nucleation in the early *C. elegans* embryo. *Dev. Cell.* 9:223–236. http://dx.doi.org/10.1016/j.devcel.2005.07.003

Srinivasan, D.G., R.M. Fisk, H. Xu, and S. van den Heuvel. 2003. A complex of LIN-5 and GPR proteins regulates G protein signaling and spindle function in *C. elegans*. *Genes Dev.* 17:1225–1239. http://dx.doi.org/10.1101/gad.1081203

Tagawa, A., C.A. Rappleye, and R.V. Aroian. 2001. *pod-2*, along with *pod-1*, defines a new class of genes required for polarity in the early *Caenorhabditis elegans* embryo. *Dev. Biol.* 233:412–424. http://dx.doi.org/10.1006/dbio.2001.0234

Tame, M.A., J.A. Raaijmakers, B. van den Broek, A. Lindqvist, K. Jalink, and R.H. Medema. 2014. Astral microtubules control redistribution of dynein at the cell cortex to facilitate spindle positioning. *Cell Cycle.* 13:1162–1170. http://dx.doi.org/10.4161/cc.28031

Tamura, N., J.E. Simon, A. Nayak, R. Shenoy, N. Hiroi, V. Boilot, A. Funahashi, and V.M. Draviam. 2015. A proteomic study of mitotic phase-specific interactors of EB1 reveals a role for SXIP-mediated protein interactions in anaphase onset. *Biol. Open.* 4:155–169. http://dx.doi.org/10.1242/bio.201410413

Timmons, L., and A. Fire. 1998. Specific interference by ingested dsRNA. *Nature.* 395:854. http://dx.doi.org/10.1038/27579

Toyoshima, F., and E. Nishida. 2007. Integrin-mediated adhesion orients the spindle parallel to the substratum in an EB1- and myosin X-dependent manner. *EMBO J.* 26:1487–1498. http://dx.doi.org/10.1038/sj.emboj.7601599

Vaughan, K.T., S.H. Hughes, C.J. Echeverri, N.F. Faulkner, and R.B. Vallee. 1999. Colocalization of cytoplasmic dynein with dynactin and CLIP-170 at microtubule distal ends. *J. Cell Sci.* 112:1437–1447.

Vaughan, P.S., P. Miura, M. Henderson, B. Byrne, and K.T. Vaughan. 2002. A role for regulated binding of p150^{Glue}) to microtubule plus ends in organelle transport. *J. Cell Biol.* 158:305–319. http://dx.doi.org/10.1083/jcb.200201029

Verbrugghe, K.J.C., and J.G. White. 2004. SPD-1 is required for the formation of the spindle midzone but is not essential for the completion of cytokinesis in *C. elegans* embryos. *Curr. Biol.* 14:1755–1760. http://dx.doi.org/10.1016/j.cub.2004.09.055

Ward, J.D. 2015. Rapid and precise engineering of the *Caenorhabditis elegans* genome with lethal mutation co-conversion and inactivation of NHEJ repair. *Genetics.* 199:363–377. http://dx.doi.org/10.1534/genetics.114.172361

Wildwater, M., N. Sander, G. de Vreede, and S. van den Heuvel. 2011. Cell shape and Wnt signaling redundantly control the division axis of *C. elegans* epithelial stem cells. *Development.* 138:4375–4385. http://dx.doi.org/10.1242/dev.066431

Xia, P., Z. Wang, X. Liu, B. Wu, J. Wang, T. Ward, L. Zhang, and X. Ding. 2012. EB1 acetylation by P300/CBP-associated factor (PCAF) ensures accurate kinetochore–microtubule interactions in mitosis. *Proc. Natl. Acad. Sci. USA.* 109:16564–16569. http://dx.doi.org/10.1073/pnas.1202639109

Zanic, M., P.O. Widlund, A.A. Hyman, and J. Howard. 2013. Synergy between XMAP215 and EB1 increases microtubule growth rates to physiological levels. *Nat. Cell Biol.* 15:688–693. http://dx.doi.org/10.1038/ncb2744

Zhang, L., J.D. Ward, Z. Cheng, and A.F. Dernburg. 2015a. The auxin-inducible degradation (AID) system enables versatile conditional protein depletion in *C. elegans*. *Development.* 142:4374–4384. http://dx.doi.org/10.1242/dev.129635

Zhang, R., G.M. Alushin, A. Brown, and E. Nogales. 2015b. Mechanistic origin of microtubule dynamic instability and its modulation by EB proteins. *Cell.* 162:849–859. http://dx.doi.org/10.1016/j.cell.2015.07.012

Zimniak, T., K. Stengl, K. Mechtler, and S. Westermann. 2009. Phosphoregulation of the budding yeast EB1 homologue Bim1p by Aurora/Ipl1p. *J. Cell Biol.* 186:379–391. http://dx.doi.org/10.1083/jcb.200901036